ISPRS Journal of Photogrammetry and Remote Sensing 202 (2023) 610–636

Contents lists available at ScienceDirect

ISPRS Journal of Photogrammetry and Remote Sensing

journal homepage: www.elsevier.com/locate/isprsjprs

A robust and unified land surface phenology algorithm for diverse biomes and growth cycles in China by using harmonized Landsat and Sentinel-2 imagery

Jilin Yang[a,b], Jinwei Dong[b,*], Luo Liu[c], Miaomiao Zhao[d], Xiaoyang Zhang[e], Xuecao Li[f], Junhu Dai[b], Huanjiong Wang[b], Chaoyang Wu[b], Nanshan You[b], Shibo Fang[g], Yong Pang[h], Yingli He[b], Guosong Zhao[i], Xiangming Xiao[j], Quansheng Ge[b,*]

[a] College of Grassland Science and Technology, China Agricultural University, Beijing 100193, China
[b] Key Laboratory of Land Surface Pattern and Simulation, Institute of Geographic Sciences and Natural Resources Research, Chinese Academy of Sciences, Beijing 100101, China
[c] Guangdong Province Key Laboratory for Land Use and Consolidation, South China Agricultural University, Guangzhou 510642, China
[d] Information Center of Ministry of Ecology and Environment, Beijing 100029, China
[e] Geospatial Sciences Center of Excellence, Department of Geography and Geospatial Sciences, South Dakota State University, Brookings, SD 57007, USA
[f] College of Land Science and Technology, China Agricultural University, Beijing, 100083, China
[g] State Key Laboratory of Severe Weather, Chinese Academy of Meteorological Sciences, Beijing 100081, China
[h] Institute of Forest Resource Information Techniques, Chinese Academy of Forestry, Beijing 100091, China
[i] School of Geography and Information Engineering, China University of Geosciences, Wuhan 430074, China
[j] Department of Microbiology and Plant Biology, University of Oklahoma, Norman, OK 73019, USA

ARTICLE INFO

Keywords:
Land surface phenology
Vegetation indices
Harmonized Landsat and Sentinel-2
30 m phenology product
China

ABSTRACT

Land surface phenology (LSP) is beneficial to understand ecosystem response to climate change, vegetation and crop type discrimination, and ecological modeling. However, the existing efforts based on coarse resolution data (≥500 m) cannot perform well in regions with higher spatial heterogeneity and multi-cropping system, such as China. Given that the majority of 10 m/30 m-based phenological research has focused on North America and Europe, developing spatiotemporally explicit LSP data in China is imperative. More importantly, the existing 30 m LSP products are mainly suitable for vegetation types with a single vegetation cycle, but cannot work well for biomes with complex seasonality (e.g., multiple growth cycles). Here we first harmonized three vegetation indices, i.e., the normalized difference vegetation index (NDVI), two-band enhanced vegetation index (EVI2), and land surface water index (LSWI) from Landsat-7/8 and Sentinel-2 imagery on the Google Earth Engine (GEE) platform. We then developed a new 30 m LSP algorithm that unified different phenological cycle-seeking processes per vegetation type and improved the existing algorithm. Furthermore, we used the algorithm to estimate the LSP product (LSP30CHN) for 2016–2019 across China, suitable for all vegetation types. The validation results showed a reasonably high accuracy ($R^2 > 0.6$, RMSE < 15 days, mostly) of the LSP30CHN data against multi-sources in-situ observational (e.g., PhenoCam) and satellite-retrieved vegetation phenology data. Moreover, LSP30CHN data showed a consistent pattern but finer spatial details with the 500 m Moderate Resolution Imaging Spectroradiometer (MODIS) phenology product (MCD12Q2) at the homogenous area. We also found that phenological differences between LSP30CHN and MCD12Q2 increased with surface fragmentation, suggesting the potential of LSP30CHN to delineate phenological information on more fragmented landscapes. In contrast, the 500 m LSP data cannot provide such details in the regions with mixed cropping structures (e.g., corn, rice, and soybean) and multiple cropping index (e.g., single- and double-cropping systems). This study offers high accuracy of the LSP map for China, valuable for finer phenology-based services such as field-level crop management and agricultural phenology monitoring. It opens up new insights about exploring large-scale refined agricultural management and ecological assessment for other regions with complicated, fragmented landscapes and vegetation seasonality.

* Corresponding authors.
E-mail addresses: dongjw@igsnrr.ac.cn (J. Dong), geqs@igsnrr.ac.cn (Q. Ge).

https://doi.org/10.1016/j.isprsjprs.2023.07.017
Received 11 March 2023; Received in revised form 25 May 2023; Accepted 14 July 2023
Available online 19 July 2023

1. Introduction

The phenological shifts of vegetation in a changing climate affect the seasonal carbon cycle (Richardson et al., 2013), agricultural production (Gao and Zhang, 2021), hydrologic processes (Zeng et al., 2017), and even bring feedback on climate change (Piao et al., 2019). Therefore, accurate phenological information is crucial for quantifying terrestrial response to climate change, agricultural production, implementing zero carbon targets (carbon neutrality) (Chen, 2021), and also contributing to land cover and land use mapping (Dong et al., 2016). The spatially and temporally continuous satellite-retrieved land surface phenology (LSP) data provide unprecedented opportunities for understanding phenological dynamics at global and regional scales. The key LSP metrics usually include the timing of the phenological events related to vegetation photosynthesis, such as the start (SOS), end (EOS), and length (GSL) of the growing season (Keenan et al., 2014; Piao et al., 2019), as well as the peak (POS) of the growing season (Yang et al., 2019).

In recent decades, the increasing archive of satellite data has greatly benefited LSP retrievals. Several LSP data products with coarse spatial resolutions have been generated and widely used by leveraging high temporal time series from multi-sensors satellite observations such as the Advanced Very High Resolution Radiometer (AVHRR, ~8km), Moderate Resolution Imaging Spectrometer (MODIS, 500 m) (Gray et al., 2019), and Visible Infrared Imager Radiometer Suite (VIIRS, 500 m) (Zhang et al., 2020a). However, those coarse resolution LSP products frequently contain a mixture of multiple vegetation types due to the limitation of their moderate spatial resolution, and thus cannot fully characterize the spatial patterns of phenological variations relevant to ecologically important processes (crop growth, forest disturbance, topography, land use, and microclimates) at the landscape scale (Bolton et al., 2020; Zhang et al., 2020b). Local-scale phenological events, especially in landscapes that are topographically complex, fragmented, or affected by human management, have not been resolved in coarse-resolution LSP products (Montgomery et al., 2020; Richardson et al., 2013). For instance, the MODIS Global Vegetation Phenology product (MCD12Q2 Version 6; MCD12Q2 hereafter) demonstrated its reliability over large regions, especially in temperate deciduous vegetation. However, the MCD12Q2 algorithm could result in failed LSP retrievals for those arid and semi-arid areas with high spatial heterogeneity and low vegetation due to its globally conservative approach (vegetation growth amplitude rule) that did not produce LSP results if the amplitude of input vegetation indices was very low (Xie et al., 2022). Therefore, new LSP data with 30 m spatial resolutions capable of resolving landscape-scale features and processes are needed (Zhang et al., 2017; Zhang et al., 2020b), which is still not clear if it is good for phenology detection.

To monitor finer LSP for the relatively heterogeneous land cover landscapes (e.g., urban areas) (Li et al., 2019) and guide fine agricultural management (e.g., smallholder farms) and assist land use mapping, the remote sensing community has increasingly focused on Landsat 30 m remote sensing imagery (Claverie et al., 2018; Melaas et al., 2013a). Various studies generated interannual variation of Landsat-retrieved LSP metrics for a given pixel by comparing annual phenological timing shifts relative to the long-term vegetation seasonality (or phenology) that was obtained from multiple-year average observations (Fisher et al., 2006; Li et al., 2019; Melaas et al., 2013b; Melaas et al., 2018; Melaas et al., 2016). This assumption of static seasonal vegetation growth amplitude and leaf expansion rate was made to suppress the limitation that Landsat time series have a few usable/valid annual observations per year which are not dense enough for function-fitting methods (Li et al., 2019; Melaas et al., 2016). There is no doubt that this approach is one of the only viable methods of retrieving moderate resolution LSP prior to the availability of abundant Sentinel-2 time series, which is of great value given the temporal depth of the existing Landsat archive. However, reliable phenological retrieval should avoid relying on time scales where surface changes are likely to occur (e.g., decades) and should be based on satellite observations in the target year to the extent possible (Bolton et al., 2020; Zhang et al., 2020b). One study retrieved a 30 m long-term (1984–2019) Landsat-based annual LSP product using the double-logistic function (DBL) fitting method and Bayesian hierarchical model (Gao et al., 2021). This product may approximately retrieve multi-year averages and yearly LSP metrics which greatly benefited phenological dynamics at 30 m spatial resolution and over the past three decades. However, it is more applicable to single-season vegetation such as deciduous forests, and may not perform well for the multi-cropping system with complex seasonality and sparse vegetation types, that result from the design of the phenology extraction model (Gao et al., 2021).

Recently, annual LSP retrieved from Sentinel-2 has proven to be feasible, thus overcoming the limitations imposed by Landsat's longer temporal resolution. The Sentinel-2 satellites at 10 m spatial and with a revisit time of 5 days aid continental-scale high-resolution LSP mapping (Drusch et al., 2012) and have been applied at local scales (d'Andrimont et al., 2020; Vrieling et al., 2018) and Europe (High-Resolution Vegetation Phenology and Productivity dataset; HR-VPP) (Copernicus, 2020; Salinero-Delgado et al., 2021; Tian et al., 2021). The core of the HR-VPP algorithm is the identification of single or double growing seasons, and then the seasonality was determined by a spline fitting to the original data before the DBL fitting (Jönsson et al., 2018; Tian et al., 2021), which is still unable to accurately fit the growth trajectory of multi-season vegetation due to the inherent limitations of the DBL on the pre-defined fitting parameters and curve shapes. Not to mention the fact that it has been pointed out that the DBL is not well suited to the EOS estimate of the crop due to time series do not closely resemble logistic growth in those in systems (Gray et al., 2019).

Sentinel-2 data provide spectral information and spatial resolution similar to Landsat data. There is a large-scale 30 m Harmonized Landsat Sentinel-2 (HLS) data product that can be used for LSP mapping, which integrates Landsat-8 (NASA) and Sentinel-2 (ESA) measurements into global observations of the land every 2–3 days at 30 m spatial resolution (Bolton et al., 2020; Claverie et al., 2018; Zhang et al., 2020b). Bolton et al. (2020) generated an HLS-based LSP data product (MSLSP30NA) for North America using the MCD12Q2-like phenological retrieval methods (i.e., smoothing spline and seasonal amplitude threshold approach). MSLSP30NA is currently only a 30 m continental-scale LSP product available from 2016 to 2019. In addition to the HLS data alternative, Zhang et al. (2020b) produced a 30 m LSP product in eight HLS tiles in the United States from a synthesized time series by fusing HLS-VIIRS data combined with the hybrid piecewise logistic model. The complicated data fusion depends on the cloud-free Landsat-MODIS image pairs available for a given region, and thus the method is still limited to the local scale (Gao et al., 2017). Technically, these annual LSP products mentioned above have been derived based on a valid vegetation cycle detection procedure that is prone to ambiguity. They all underperform more or less in multi-season vegetation patterns. For example, MCD12Q2 and MSLSP30NA products have a considerable misestimate on the identification of the leaf emergence/senescence stage of winter crops such as winter wheat (Liu et al., 2020). These algorithms often identify the leaf emergence stage as the green-up stage due to their limited robustness (Fig. S1; see Section 2.4.2). That is, if the amplitude ratio of a vegetation cycle during the overwintering period is >35% in many winter wheat, the cycle will be misidentified by these LSP algorithms as true, resulting in the wrong SOS or EOS (Fig. S1). On the other hand, although several 30 m LSP products have been produced, large-scale multi-source efforts are rare because the procedures are data-demanding and computationally intensive (Claverie et al., 2018). Fortunately, cloud-based distributed data/processing platforms, such as the Google Earth Engine (GEE), a planetary-scale geospatial analysis platform, have provided an unprecedented opportunity to address the contradiction between the demand for fine phenological applications and the inadequate supply of fine LSP products (Descals et al., 2021; Gorelick et al., 2017; Salinero-Delgado et al., 2021).

Researchers and policymakers in every country or region want to get a better understanding of accurate LSP information and its spatial variation. At present, such information is either unavailable or available in a very coarse spatial detail. Given that the majority of phenological research has focused on North America and Europe, this is important to develop spatiotemporally explicit 30 m LSP data in China related to spatial patterns of local variability. Mapping LSP at 30 m resolution is an opportunity that can be addressed by 30 m rather than 500 m data in China. The land surface in China is characterized by an intricate patchwork of fragmented landscapes (e.g., crop fields with asynchronized phenology) with highly fragmented land use and dramatic land-use change, and great human influence (Li et al., 2019; Qiu et al., 2020b). On the other hand, the production of 30 m LSP is also challenging in China. The Chinese terrestrial surface has more extensive, complex, and diverse vegetation cycles and cropping systems (e.g., single and double cropping) (Liu et al., 2014), unlike areas (e.g., North America) with 30 m LSP data products where single cropping system are almost uniform and double cropping crops are rare (Fig. S2) (Bolton et al., 2020; Friedl et al., 2019). There are multiple attempts to retrieve the 30 m LSP in local areas of China. The multiple vegetation cycles of crop vegetation were portrayed by using a single vegetation index (Niu et al., 2022; Pan et al., 2015; Qiu et al., 2020a) or combining multiple vegetation indices that work together to characterize the state of the land surface (Liu et al., 2020), which were carried out at small-scale and for a single vegetation type. For example, Pan et al. (2015) mapped crop LSP using 30 m HJ-1 A/B remote sensing imagery derived from China Environment Satellite in Guanzhong Plain in Shaanxi Province, China. One major drawback is that the large-scale production and application of LSP products based on Chinese high-resolution satellites, such as HJ and GF, is very difficult due to the lack of unified standardized preprocessing (topographic and atmospheric correction, etc.) and data sharing. Furthermore, it is difficult to design an algorithm to be applicable to multiple vegetation types over large areas. The current phenological algorithms for the 30 m landscape-scale proposed in previous studies are applicable to either a single-cycle vegetation type (Liu et al., 2020; Pastick et al., 2020; Wang et al., 2020; Zhang et al., 2022) or multiple-cycle systems at local scales (Liu et al., 2020; Wang et al., 2020; Zhang et al., 2020b). Despite existing efforts in multiple cycles in the coarse resolution image-based analyses (Gray et al., 2019; Zhang et al., 2020a), it is still unclear whether those are good for phenology detection in China, and a unified algorithm for the 30 m LSP retrieval algorithm for different vegetation, including diverse vegetation cycles, is unavailable.

To close these knowledge gaps, we aim to develop and evaluate a new unified algorithm for vegetation phenological retrieval across biomes, designed to fill the above gaps and generate a 30 m LSP product at broad scales by integrating Landsat-7/8 and Sentinel-2 time series (Fig. 1). The main objectives of this study are: (1) To present a new algorithm embedded in the GEE platform for estimating landscape-scale LSP metrics from Landsat-7/8 and Sentinel-2 satellite imagery in China; (2) To describe and characterize an LSP data product (LSP30CHN) based on the proposed algorithm; and (3) To validate the LSP30CHN product using multi-source in-situ measurements of

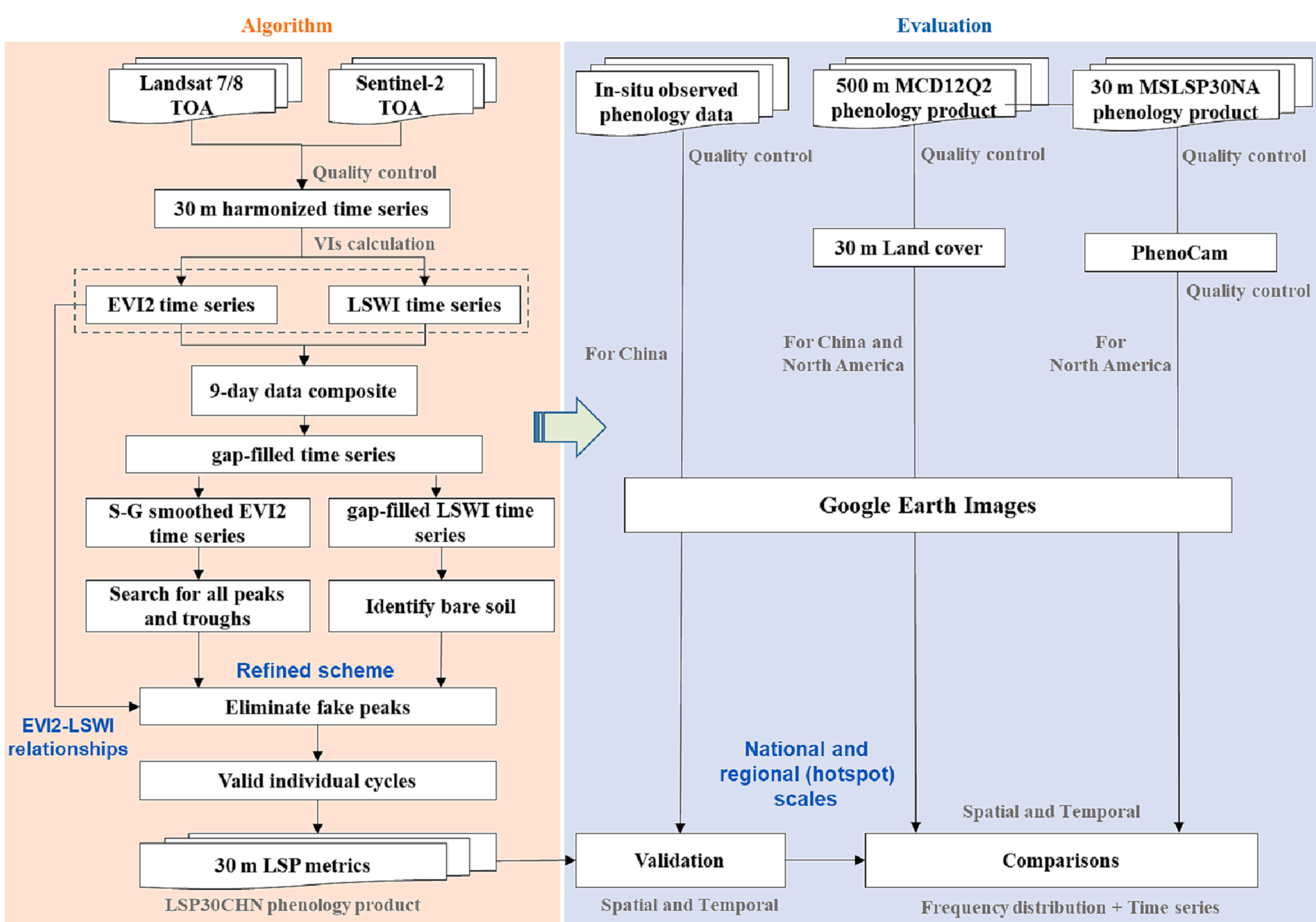

Fig. 1. Flowchart illustrating production and validation of our new algorithm for generating 30 m land surface phenology from combined Landsat-7/8 and Sentinel-2 time series. Please see Table 1 for more data specifications. In order to ensure the scalability and robustness of our algorithm, although MSLSP30NA data product was only for North America, we still used it to make a comparison with our product in North America (see Section 2.5.2 for details). TOA: top-of-atmosphere reflectance. S-G: Savitzky–Golay filter, a data smoothing method.

phenology and to implement comparisons with frequently-used satellite-retrieved LSP data products.

2. Materials and methods

2.1. Overview of the phenological metrics retrieval

We used a two-band enhanced vegetation index (EVI2) time series from the integrated Landsat-7/8 and Sentinel-2 imagery for LSP retrieval in China at 30 m resolution, due to its ability to eliminate the background and atmosphere noises and its non-saturation, a typical NDVI problem (Huete et al., 2002; Zhang et al., 2020b). Here we targeted a unified algorithm across biomes with diverse vegetation cycles (Fig. 1), including 1) integration of EVI2 time series in 2016–2021 from Landsat-7/8 and Sentinel-2 datasets, 2) gap-filling and smoothing the noisy EVI2 time series, 3) identifying valid vegetation cycles in EVI2 time series, 4) estimation of phenological metrics (i.e., SOS, EOS, GSL, and POS), and 5) validation/comparison of phenological retrievals. The detailed processing description was as follows.

2.2. Data and preprocessing

2.2.1. Landsat and Sentinel-2 data

We used the integrated Landsat-7/8 and Sentinel-2 imagery for LSP retrieval in China at 30 m resolution. The Collection 2 calibrated top-of-atmospheric (TOA) reflectance data during 2016–2021, hosted on the GEE platform, were used in this study (Fig. S3). TOA reflectance data were obtained from Landsat-7 Enhanced Thematic Mapper Plus (ETM+), Landsat-8 Operational Land Imager (OLI), and the Sentinel-2A/2B MultiSpectral Instrument (MSI) orthorectified TOA reflectance (Level-1C) (Table 1). The winter crops (e.g., winter wheat and winter rapeseed) whose vegetation cycles are always across calendar boundaries, are widely distributed in China (Dong et al., 2020; Liu et al., 2020). To reduce uncertainty due to land cover land use change, the computation period is shrunk in our algorithm while ensuring that we included all the growth characteristics of the vegetation as much as possible. For each target year, 6 months of the preceding year, 12 months of the target year plus 3 months of the subsequent year, a total of 21 months were selected for phenological estimation. In this study, we chose to study the period from July 2015 to March 2022 for 2016–2021. For example, considering 2019 as the target year, we selected data from July 2018 to March 2020. All poor-quality observations that were unrelated to vegetation signals were identified, including cloud, cloud shadows, cirrus, and snow/ice, as well as Landsat-7 ETM + scan line corrector (SLC)-off gaps (Arvidson et al., 2006; Chen et al., 2011). These invalid observations were identified by the quality assurance (QA) flags, which used the FMask algorithm (Foga et al., 2017; Zhu et al., 2015), and were reduced for individual sensors (ETM+, OLI, and MSI).

We calculated the spatial and frequency distributions of all observations and valid (i.e., good-quality) observations, respectively. Fig. 2 showed the spatial distributions of the number of valid observations in the study period across China from the combined Landsat-7/8 and Sentinel-2 TOA datasets. The combined Landsat/Sentinel data can guarantee at least one valid observation per month for implementing our phenological algorithm (Fig. 2 d-f).

2.2.2. Land cover datasets

The Global Land Cover with Fine Classification System at 30 m resolution in 2020 (GLC_FCS30-2020) data product (hereafter 30 m-LC) was used to determine the scaling effect in this study. The 30 m-LC is developed on the GEE platform by integrating the 2019–2020 Landsat surface reflectance (SR) data, Sentinel-1 SAR data, DEM terrain elevation data, global thematic auxiliary dataset, prior knowledge dataset, and local adaptive random forest model (https://zenodo.org/record/4280923#.YQ-mfOgzap0). The 30 m-LC data provide the classification scheme of 30 classes similar to the Climate Change Initiative Land Cover (CCI-LC) data. The overall accuracy of 30 m-LC was >68% with a kappa coefficient of about 0.67 (Zhang et al., 2021b). Six land cover classes were merged from the original classes into forests, shrublands, grasslands, savannas, croplands, and non-vegetation. The croplands class contains 4 subclasses, i.e., rainfed cropland, herbaceous cover, tree or shrub cover (orchard), and irrigated cropland.

In addition to 30 m-LC data for natural vegetation, to assist in the correction of in-situ observation sites, we used multiple published vegetation type data products at 10 m/30 m resolution in China, including winter wheat (Dong et al., 2020), summer maize (Niu et al., 2022; You et al., 2021), single- and double-cropping rice (He et al., 2021; You et al., 2021; Zhang et al., 2021a).

2.2.3. 500 m MCD12Q2 LSP data product

The LSP metrics for 2016–2019 were obtained from the MODIS Land Cover Dynamics (MCD12Q2 Collection 6) product (Gray et al., 2019). MCD12Q2 data were produced at 500 m from EVI2 time series calculated from daily normalized MODIS Nadir BRDF-Adjusted reflectance data (version 6) (https://lpdaac.usgs.gov/products/mcd12q2v006) (Gray et al., 2019) and MCD12Q2 is only available through 2019. The SOS and EOS dates (i.e., 'Greenup', and 'Dormancy' layers in the product) used in this study are defined as the dates when EVI2 first and last crossed 15% of the EVI2 amplitude in the growing cycle, respectively (Gray et al., 2019).

Table 1
Input and validation datasets used in this study and their specifications.

Dataset	Derived Variables	Spatial Resolution	Temporal Duration	Temporal Resolution	Reference URL
Landsat-7 TOA	EVI2 NDVI LSWI	30 m	2015.07.01–2022.03.31	16-day	https://www.usgs.gov/core-science-systems/nli/landsat/landsat-surface-reflectance
Landsat-8 TOA	EVI2 NDVI LSWI	30 m	2015.07.01–2022.03.31	16-day	https://www.usgs.gov/core-science-systems/nli/landsat/landsat-surface-reflectance
Sentinel-2 TOA	EVI2 NDVI LSWI	10 m/20 m	2015.07.01–2022.03.31	5-day/ combined constellation	https://earth.esa.int/web/sentinel/user-guides/sentinel-2-msi/product-types/level-2a
GLC_FCS30-2020	Major land cover type	30 m	2020	yearly	https://zenodo.org/record/4280923#.YQ-mfOgzap0
PhenOBN	Manually observed LSP	In-situ	2019	yearly	Upon reasonable request
PhenoCam	GCC-based LSP	In-situ	2016–2018	yearly	https://doi.org/10.3334/ORNLDAAC/1674
MCD12Q2v6	EVI2-based LSP	500 m	2016–2019	yearly	https://lpdaac.usgs.gov/products/mcd12q2v006/
MSLSP30NAv001	EVI2-based LSP	30 m	2016–2019	yearly	https://lpdaac.usgs.gov/products/mslsp30nav001

Note: TOA: top-of-atmosphere reflectance. NDVI: the normalized difference vegetation index, EVI2: 2-band enhanced vegetation index, LSWI: land surface water index. PhenOBN: In-situ phenological observation datasets for China collected in this study (see Section 2.2.5). GCC: green chromatic coordinate index. MCD12Q2 phenology data is derived from daily MODIS normalized BRDF-adjusted reflectance data (version 6) and provided by NASA LP DAAC at the USGS EROS Center at a 500 m spatial resolution (see Section 2.2.3).

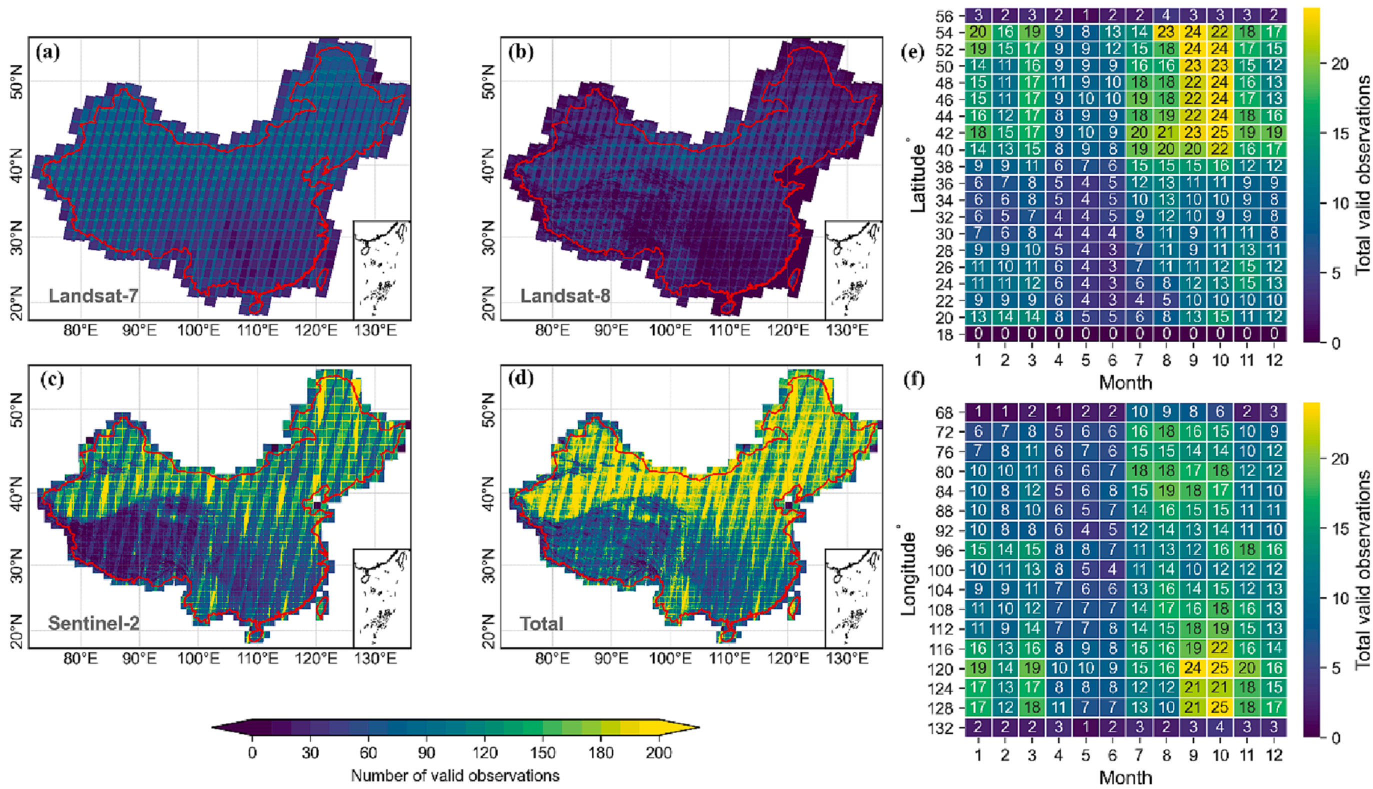

Fig. 2. Valid observations numbers for three sensors for a total of 21 months from July 2018 to March 2020. Landsat-7 (a), Landsat-8 (b), Sentinel-2 (c), and a total of three sensors (d), as well as monthly total valid observations along latitude (e) and longitude (f) gradients, respectively.

2.2.4. 30 m MSLSP30NA LSP data product

The MSLSP30NA (version v011) phenology data product provides yearly LSP phenological metrics from 2016 to 2019 at 30 m resolution for North America (Bolton et al., 2020; Friedl, 2020). It was generated from the HLS EVI2 time series using a smoothing spline (Migliavacca et al., 2011) and seasonal amplitude threshold approach (Friedl, 2020). All poor-quality pixels of the MSLSP30NA product were excluded using its QA bands. We then compared the SOS and EOS in our LSP30CHN product with the OGI (date of 15% greenness increase) and OGD (date of 10% greenness decrease) layers in the MSLSP30NA product, respectively.

2.2.5. Field phenological observations data

The in-situ phenological observations data were collected from three

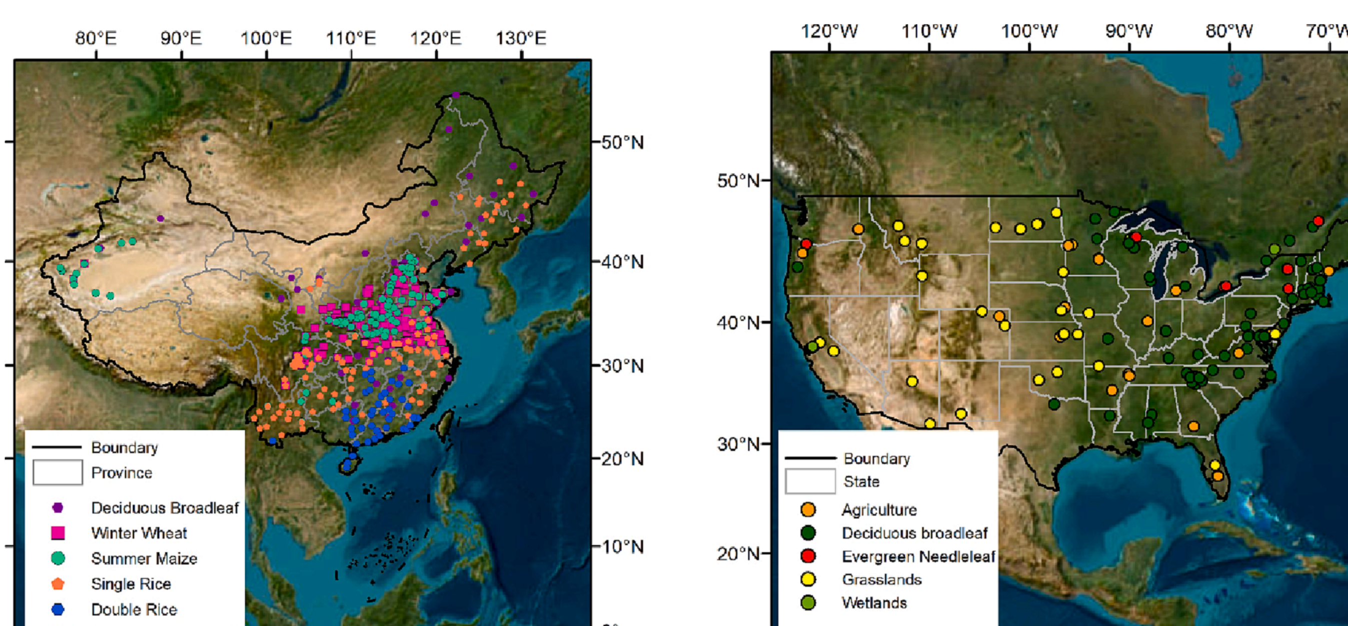

Fig. 3. Spatial distributions of 411 and 170 in-situ phenological observation stations in China (a) and North America (b), respectively. It should be noted that the phenological data are different between China (dates of phenological events) and the North America (PhenoCam).

phenological observation networks (hereinafter, PhenOBN) in China that were only available for 2019 in this study, including the Chinese Forest Ecosystem Research Network (CFERN), Chinese Phenological Observation Network (CPON), and Chinese Agricultural Meteorological Monitoring System (CAMMS) based on local agro-metrological observation stations. A total of 411 stations were collected for 2019 across China after strict data quality control, including 49 forest stations (deciduous broadleaf forests) and 362 croplands stations (Fig. 3 a). In this study, considering the typicality of growth curve characteristics, crop types such as winter wheat, summer maize and rice were selected for validation (see Text S1 for more information of dominant cropland in China).

Well-trained technicians in the experimental fields observed and recorded all phenological records and then checked and managed following the uniform regulations on these above operations for individual observation networks (Ge et al., 2015). Each station of the PhenOBN database contains several plant species and their growth stages, and the phenological metrics (SOS or EOS) across all individual species were averaged for each station. It should be pointed out that we manually corrected the coordinates of all PhenOBN observation stations one by one as their locations were not always precise for individual records. Specifically, we created a 5 km buffer around each station and overlaid high-resolution vegetation cover data (Section 2.2.2), which marked the target vegetation types involved in this study. We then found a window of pixels (pixel window) closest to the station within this buffer on high-resolution vegetation cover data. The pixel window was required to have at least 12 × 12 pixels of the target vegetation types at 30 m resolution distributed continuously which corresponds to 3/4 of a 500 m MODIS pixel. Finally, the final coordinate of the station was updated as the centroid of the pixel window (Fig. S4).

It should be noted that to achieve a consistent definition of vegetation phenology at a national scale, the definition of SOS of our product is the same as those of both MODIS and MSLSP30NA datasets. That is, the SOS of the overwintering vegetation designated for the three products is the emergence date, all of which are in the previous year. For example, the SOS of winter wheat was the leaf emergence of the previous year (e.g., 2018 autumn) to make it clear that the SOS of all vegetation types is at the beginning of a complete vegetation cycle (Table 2). Therefore, in this study, as for SOS dates, we used the leaf emergence dates for the forest, winter wheat, and summer maize while the tillering dates were for single rice and double rice. In terms of EOS dates, we used the leaf senescence dates for the forest and maturity dates for all of the above four crops, respectively (Table 2).

2.2.6. PhenoCam data

The PhenoCam Dataset v2.0 covering the period 2016–2018 was used in this study to validate our proposed algorithm. The PhenoCam Network collects high-frequency automated visible-wavelength (red, green, blue) digital camera imagery at each site across North America and Europe from 2000 to 2018 (Seyednasrollah et al., 2019b). The phenology data were derived from the time series of the green chromatic coordinate index (GCC = Green/(Blue + Red + Green)) over 1- and 3-day temporal intervals. The GCC characterized vegetation color and canopy greenness and was calculated for a region-of-interest (ROI) that delineates an area of specific vegetation type.

We first selected PhenoCam sites covering North America, and then conducted GCC quality checks site by site according to the field of view (FOV) of the region of interest (ROI) and manually adjusted the site locations to ensure that they aligned with the vegetation type being observed (Fig. S5). For those sites whose location does not match phenoCam FOV, we corrected this by moving the site location appropriately according to FOV and ROI (Fig. S5 a-d). For those sites whose GCC curves were not of good quality (Fig. S5 e-f) or whose camera observations were not canopy information (Fig. S5 g-h), we excluded them. In total, 170 PhenoCam stations with a total of 384 site-years were included in the validation (Fig. 3 b; Table 3). The definitions of transition_25 and transition_25 date when GCC series data crossed 25% and 25% of the GCC were used to determine the SOS and EOS from PhenoCam, respectively (Richardson et al., 2018a). We chose North America because no satisfactory PhenoCam data are available in China. The same phenological approach adopted in China for various vegetation types was used in North America where PhenoCam data are accessible. Thus, this compromise method can be used as a supplementary validation of our algorithm, because it can reduce the imbalance of the proportion of various vegetation types of sites used in China. Meanwhile, the feasibility of our approach can be evaluated through this method.

2.2.7. Chinese ecosystem research network

In this study, we only used the coordinate locations of the 6 Chinese Ecosystem Research Network (CERN) sites to extract the results of LSP30CHN and MCD12Q2 products. These sites were carried out under the CERN framework following uniform standards and were related to six vegetation types, such as deciduous broadleaf forests, evergreen broadleaf forests, grasslands, winter wheat, summer maize, and single rice. Moreover, the landscape of these locations was spatially homogeneous and their location was constant over time, to confirm the temporal consistency of our algorithm and MODIS products, as well as the robustness of inter-annual variations of phenological metrics (refer to Fig. S6 for details).

2.3. EVI2 and LSWI time series from harmonization of Landsat and Sentinel-2 data

2.3.1. Harmonization of Landsat and Sentinel-2 data

Due to the differences in spectral bandwidth among ETM+ (Landsat-

Table 2
Summary of in-situ phenological data in China investigated in the study.

Vegetation types	SOS record field/year	EOS record field/year	stations/No. of records
winter wheat	emergence/2018	maturity/2019	127/127
summer maize	emergence/2019	maturity/2019	84/84
single rice	tillering/2019	maturity/2019	107/107
double rice	tillering/2019	maturity/2019	44/44
deciduous broadleaf forests	emergence/2019	senescence/2019	49/1556

Note: The 'record field' denotes the phenological metrics records of 411 in-situ station-based observations used in this study. SOS/EOS denotes the start/end of the growing season. In general, the leaf emergence of winter wheat occurs in the autumn of the previous year, and the green-up occurs in the spring of the following year. To match phenological metrics with all LSP data products, we use the emergence date as SOS for winter wheat in this study. The single-cropping rice (i.e., single rice) refers to early rice, middle rice, or late rice, while double-cropping rice (i.e., double rice) represents an early rice-late rice rotation, a cropping-rotation system.

Table 3
Description of in-situ PhenoCam data used in this study.

Vegetation Types	Description	SOS/year	EOS/year	No. of Sites/ Site-years
DB	deciduous broadleaf forests	emergence/ 2019	maturity/ 2019	69/174
EN	evergreen needleleaf forests	emergence/ 2019	maturity/ 2019	10/27
GR	grasslands	emergence/ 2019	maturity/ 2019	31/64
AG	agriculture	emergence/ 2018, 2019	maturity/ 2019	54/106
WT	wetlands	emergence/ 2019	maturity/ 2019	6/13

7), OLI (Landsat-8), and MSI (Sentinel-2) sensors, remote sensing data should be harmonized to obtain comparable reflectance values to improve the consistency of the Landsat and Sentinel-2 TOA reflectance (Liu et al., 2020; Zhang et al., 2018a). Given NASA-based HLS data was not hosted on GEE, so it is not used in this study. Instead,we harmonized and combined Landsat ETM+, OLI, and Sentinel MSI imagery by adjusting the spectral bands of ETM+ and MSI to match those of OLI data (as a reference) using a linear regression approach which has been widely used to reduce the reflectance difference between the two similar satellite observations (Claverie et al., 2018; Roy et al., 2016; Zhang et al., 2018a). Specifically, for Landsat-7 data, bands 3 (Red), 4 (near infrared, NIR), and 5 (shortwave infrared, SWIR) were transformed using correction coefficients derived from the ordinary least squares regression (Table 4). For Sentinel-2 data, as the wavelength (NIR) of band 8A matched that of OLI better, the bands 4 (Red), 8A (NIR), and 11 (SWIR) were thus selected and transformed (Zhang et al., 2018a) (Table 4). Moreover, Sentinel-2 data were resampled to 30 m × 30 m using bicubic resampling to ensure consistent spatial resolution with Landsat-7/8 data, reducing the differences generated by spatial resolution. Then we merged these three datasets by their acquisition time and constructed a comparable TOA time series (see Fig. S7 for their matching performance and Fig. S8 for seasonal comparison between NASA-based HLS and HLS used in this study).

2.3.2. Calculation of three vegetation indices

Three vegetation indices (VIs), i.e., the normalized difference vegetation index (NDVI), EVI2 (Huete et al., 2002; Jiang et al., 2008), and land surface water index (LSWI) (Xiao et al., 2005), were calculated for each sensor, respectively. In our new algorithm, the EVI2 time series was used to extract the phenological metrics, while NDVI and LSWI time series were used to eliminate invalid EVI2 values. In addition, LSWI also was used to determine the valid vegetation cycles by identifying the false peaks (Liu et al., 2020; Xiao et al., 2006). Detailed operations were described below. We used the EVI2 time series to develop the phenological algorithm due to its ability to eliminate the background and atmosphere noises and its non-saturation, a typical NDVI problem (Huete et al., 2002; Zhang et al., 2020b). NDVI and LSWI were used to further eliminate invalid EVI2 values. In this study, the corresponding NDVI values were collected to identify those observations with LSWI > NDVI as flooding/snow-contaminated observations that need to be removed (Zhang et al., 2018b). LSWI of these contaminated observations usually will be high and larger than NDVI because the reduction in SWIR is much higher than that in the NIR band (Fig. S9 a-c). On the other hand, high anomalous EVI2 values in time series may arise from spuriously low red band values caused by multiple influencing factors (Zhang et al., 2018b), which we effectively eliminate by comparing with NDVI values (Wang et al., 2015; Zhang et al., 2018b). Specifically, EVI2 values >90% of the co-occurring NDVI values are identified as anomalous ones (Zhang et al., 2018b) (Fig. S9 d-e).

Furthermore, to focus on the areas with vegetation seasonality, a pixel was excluded if the mean (and maximum) EVI2 value during the growing season (from May to September) was lower than 0.1 (and 0.12) considered low vegetation (Huete et al., 2002; Jeong et al., 2011; Piao et al., 2006). The growing season here was a broad concept based on the average growing season of vegetation in the Northern Hemisphere although the length of a growing season varies from place to place (Xu et al., 2016). An additional filtering condition was added in this study, which would further effectively exclude non-vegetation and low/sparse vegetation. If the maximum value of EVI2 corresponding to LSWI > 0 was < 0.1, then this pixel should also be discarded. Moreover, to reduce the impact of the bad quality of Sentinel-2, those Sentinel-2 data would be eliminated if the granule-specific cloudy pixel percentage is > 80% and the mean solar zenith angle was > 85°.

$$NDVI = \frac{NIR - Red}{NIR + Red} \tag{1}$$

$$LSWI = \frac{NIR - SWIR}{NIR + SWIR} \tag{2}$$

$$EVI2 = 2.5 \times \frac{NIR - Red}{NIR + 2.4 \times Red + 1} \tag{3}$$

where *Red*, NIR, and SWIR are the TOA reflectance values from the *Red*, *NIR*, and SWIR spectral bands, respectively (Table 4).

Table 4
The top-of-atmosphere (TOA) reflectance sensor transformation relations (ETM+ / MSI to OLI) are derived by ordinary least squares (OLS) regression of the data.

Bands #	Landsat-7	Bands #	Sentinel-2
Blue	OLI = 0.0173 + 0.8707 × ETM+	Blue	OLI = 0.0154 + 0.8729 × MSI
Red	OLI = 0.0107 + 0.9175 × ETM+	Red	OLI = 0.0066 + 0.9103 × MSI
NIR	OLI = 0.0374 + 0.9281 × ETM+	NIR (Band 8A)	OLI = 0.0056 + 0.9701 × MSI
SWIR	OLI = 0.0260 + 0.9414 × ETM+	SWIR	OLI = 0.0019 + 0.9668 × MSI

Note: Bandwidths (nm) for each sensor are as follows. Landsat-7: Blue (450–520), Red (630–690), NIR (770–900), and SWIR (1550–1750) bands. Landsat-8: Blue (452–512), Red (636–673), NIR (851–879), and SWIR (1566–1651) bands. Sentinel-2: Blue (496.6 (S2A)/492.1 (S2B)), Red (664.5 (S2A)/665 (S2B)), NIR (864.8 (S2A)/864 (S2B)), and SWIR (1613.7 (S2A)/1610.4 (S2B)) bands. S2A denotes Sentinel-2A while S2B denotes Sentinel-2B.

2.3.3. Composition of vegetation indices data and outlier removal

Even though the EVI2 values filtered by the quality assurance (QA) flags are supposedly high quality, the EVI2 time series still contain negatively biased values due to abiotic contamination such as cloudy and atmospheric effects (Shen et al., 2015). Besides, due to swath overlap (or sidelap) from each sensor and/or among sensors (Fig. 2), the VIs values in one pixel across sensors or overpass time usually vary. Therefore, we further composited EVI2 with a 9-day interval by calculating the maximum (and average) of all possible observed EVI2 (and LSWI) values, respectively, to reduce the influence of cloud/snow and generated EVI2 and LSWI time-series data at a regular interval for the next step of fitting operation (Liu et al., 2020).

Since the EVI2 value was often lower, while the LSWI may be slightly higher when clouds or aerosols are present, we used different strategies to gap-fill these two VIs. Specifically, the maximum EVI2 value is adopted in the 9-day composition, not only to eliminate the negative bias effect of cloud and cloud shadow on EVI2 but also to avoid these effects caused by the mismatch between different sensor data during harmonization (i.e., one sensor may have the lowest EVI2 data that needs to be eliminated). On the other hand, in some cloudy/rainy areas and two-season cropping systems, combined with the limited number of valid observations, the LSWI signal may be masked by the maximum and/or mean of the 9-day time window. To ensure that the bare soil can be captured as much as possible, we adopt the LSWI value of the minimum value within the 9-day composition window (window_size).

Moreover, a modified outlier identification/removal procedure based on a moving window was applied to remove the outliers in the EVI2 time series after the composition. We set the moving window size to 5. If the EVI2 value of the center point within the window was higher than three times the standard deviation of the mean value of the other four data points around it, then the EVI2 value of the center point would be replaced with the mean of the other data points. EVI2 values at data center points were not recognized as outliers and were not replaced in three situations as followed (Fig. S9 f).

(1) If the EVI2 value of the center point is higher than the 35% quantile of the entire EVI2 time series of the target year, then the EVI2 of the center point is not updated. This step was mainly to avoid the peak

being replaced.

(2) If there is no data for the center point or if at least one point to the left and right of the center point has no data, then no update.

(3) The first two and last two data points of the entire time series of the target year didn't need to be updated.

2.3.4. Gap-filling and smoothing the EVI2 time series data

Good-quality observations are often not available in some regions and times due to the effect of clouds/shadows, aerosols, snow, and/or sensor degradation or failure, resulting in some gaps in the EVI2 time series. The linear interpolation based on high-quality data before and after the time step was used to fill these gaps. The EVI2 curve, in theory, should be continuous and smooth due to the narrow range of plant growth in the 9-day interval (Zhang et al., 2018b), however, residual noise can persist in the dataset even after compositing images and the elimination of bad-quality observations, and thus leads to the non-negligible fluctuations in the EVI2 curve. We adopted the Savitzky–Golay (S-G) filter to reconstruct the EVI time series using a moving window with an original size of 9 observations and a polynomial order of 2, based on the trade-off between fitting accuracy and smoothness (Chen et al., 2004; Yang et al., 2019). The window size was selected referred on the literature (Liu et al., 2020; Zhang et al., 2022). It should be noted that we did not smooth the LSWI time series since LSWI varies dramatically during the dry-wet transition, and the smoothing operation is not appropriate (Liu et al., 2020). The original EVI2 and LSWI time series and the fitted EVI2 and gap-filled LSWI datasets were prepared for further phenological retrieval.

Fig. 4 showed the reconstruction of EVI2 seasonal trajectories harmonized from Landsat and Sentinel-2 EVI2 time series for eight randomly selected ecosystems: deciduous broadleaf forest, evergreen broadleaf forest, grasslands, wetlands, winter wheat, single rice, double rice, and winter rapeseed. The harmonized Landsat and Sentinel-2 EVI2 time series for these eight examples effectively delineated the seasonal dynamics of vegetation growth regardless of the number of vegetation cycles, demonstrating the ability of reconstructed EVI2 time series to identify a range of different phenological dynamics. Overall, with the above guarantee, the S-G fitted curves can effectively capture the seasonal variances of different vegetation types, especially for multiple growing seasons.

2.4. Land surface phenology algorithm based on a refined vegetation cycle-seeking process

Previous studies have shown that depending solely on the temporal duration and amplitude of the vegetation index is insufficient for the identification of the vegetation cycle for all vegetation types (Bolton

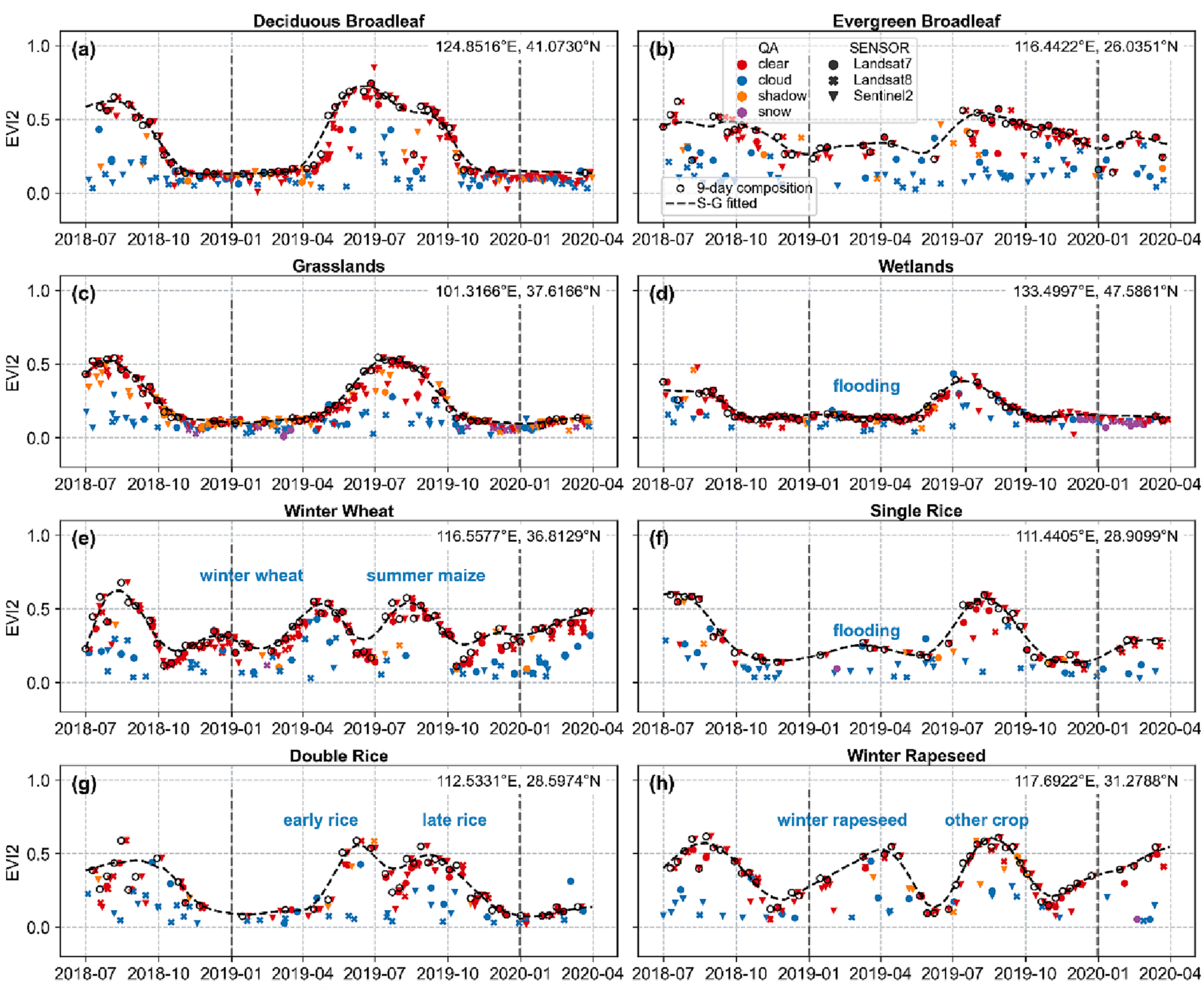

Fig. 4. Examples of harmonized 30 m EVI2 time series for the eight randomly selected forests, grasslands, and cropland sites. Each subplot shows the original time series of EVI2 with different quality levels (QA = clear, cloud, and snow) across three sensors (SENSOR = Landsat-7, Landsat-8, and Sentinel-2), respectively. The start and end of the target year (in 2019, for example) are marked by two vertical dashed gray lines. The black dashed curve indicates a fitted curve using the S-G filter method.

et al., 2020; Liu et al., 2020) (Figs. 5, 6). Because it tends to increase the risk of omission (Fig. 6 e, h) and commission (Fig. 6 a, i) for the determination of valid vegetation cycles. Therefore, it is necessary to identify the true cycles more accurately by combining multiple vegetation indices and their correlations (Liu et al., 2020) (Figs. 5, 6). As indicated in the workflow chart, we refined the valid cycle identification procedure and proposed a robust phenological metrics extraction algorithm applicable to all vegetation types, such as forests, shrublands, grasslands, and croplands (Figs. 1, 5). The core of our algorithm focused on identifying valid vegetation cycles through the analysis of EVI2 and LSWI time series.

2.4.1. Identification of valid vegetation cycles

A valid vegetation cycle (i.e., phenological cycle) is identified as a period in which the EVI2 curve exhibits specific patterns. These patterns include the rise starts rising from the leaf emergence (SOS) until it reaches the maximum during the peak growth (POS) and declines in the senescence (EOS) until it enters the dormant stage (Fig. 5 a, b). A valid vegetation cycle is characterized by a single peak and two troughs, referred to as the left and right troughs. These troughs determine the scope of vegetation phenology (Gray et al., 2019; Zhang et al., 2018c). Therefore, growing seasons dividing is a crucial prerequisite for underpinning accurate extraction of phenology, particularly inmulti-season cropping systems. To accommodate diverse vegetation types with varying growing seasons, such as single/double cropping crops and annual/deciduous vegetation, we proposed a unified peak-seeking-based method to identify all valid vegetation cycles for a given pixel, regardless of the vegetation type (Fig. 5 c). The identification process comprises following five steps.

(1) All peaks (and troughs) in the S-G fitted EVI2 curves were identified as the day of year (DOY) where the local slope of EVI2 time-series changed sign from positive to negative (or vice versa). These identified points were considered as candidate peaks ($peak_{Can}$) and candidate troughs ($trough_{left,Can}$, and $trough_{right,Can}$). These identified cycles were designated as the candidate cycles corresponding to each candidate peak. The timings of the $peak_{Can}$, $trough_{left,Can}$, and $trough_{right,Can}$ were marked as $DOY_{peak,Can}$, $DOY_{Ltrough,Can}$, and $DOY_{Rtrough,Can}$, respectively (Fig. 5 a, b).

(2) Technically, within a vegetation cycle, the smoothed EVI2 temporal profile often retained pseudo peaks and/or their corresponding troughs due to minor abiotic or biotic-induced fluctuations. As a result, multiple EVI2 waves may occur within a single vegetation cycle. Hence, it is imperative to remove these spurious cycles associated with non-vegetation growth from the candidate cycles mentioned above (Fig. 5 a). To determine the valid vegetation cycles for individual pixels, irrespective of vegetation type, we employed the following conditions for chronological iteration of each candidate cycle (Fig. 5 c). The MCD12Q2 algorithm necessitates that the amplitude of the true peak exceeds 0.1. However, several studies have indicated that this threshold may lead to the exclusion of a substantial number of pixels in semi/arid areas where the amplitude variation does not surpass 0.1 (Xie et al., 2022) (Fig. 6 d). On the other hand, in certain multiple cropping systems found in Southern China, such as the double-cropping rice system with a succession of early and late rice crops, there can be a very brief time interval of as little as two weeks between harvesting the early rice in the preceding season and transplanting the late rice in the subsequent season (Fig. 6 g, h, July in 2019). During the short time period, if satellite observations were not avaliable, the corresponding EVI2 values may not accurately capture the signals from bare ground or soil. As a result, the EVI2 amplitude ratio can be $\leq$ 35%, leading to an incorrect classification of the early rice cycle as a false cycle in the MCD12Q2 algorithm (Bolton et al., 2020). Therefore, to address the limitations of existing LSP algorithms, we have developed and implemented three parallel criteria (ConT1, ConT2, and ConT3) for accurately determining true peaks. These refined criteria are specifically designed to adapt to various complex scenarios and overcome the shortcomings of the existing methods. Specifically,

True peak condition (1) (ConT1): To identify the true peak within a cycle, the following conditions are considered:

a) The ratio (RA_{right}) of the EVI2 amplitude (A_{Right}) of the right trough to the maximum amplitude of the target year (A_{Max}) should begreater than 35%.

b) The EVI2 value ($EVI2_{Right}$) of the right trough should be lowerthan the EVI threshold ($EVI2_{thld}$), or the LSWI value of theright trough ($LSWI_{Right}$) should be<0.

If these conditions are met the peak is classified as the true peak, and consequently, the right trough is considered the true trough. This condition is effective in identifying the true peak in most cases for peaks occurring in the target year (Fig. 6 a-f, S1).

In this condition, the MCD12Q2 algorithm was utilized, which considers an amplitude ratio rule ($RA_{right} \geq 35\%$) to identify true peaks. However, in practice, peak occurring during the overwintering period, such as winter wheat, may have an amplitude ratio higher than 35%, even up to 50%. It should be noted that not all peaks with high amplitude ratios can be considered as true peaks. Therefore, it is evident that false cycles cannot be completely eliminated by solely relying on the EVI2 amplitude criterion(Fig. 6 a). Regarding winter crops with vernalization periods, such as winter wheat and winter rapeseed, a decrease in the EVI2-induced peak can be considered a a false peak and should be excluded from the analysis (Fig. 5 c, 6 a, b, f). The initiation and termination of a valid crop cycle correspond to the sowing and harvesting periods, respectively, duringwhich the surface was exposed to bare soils. In the transition period between consecutive growing seasons, the bare soils, sometimes covered with crop residues, exhibited very low very low EVI2/LSWI values (Low EVI2 and/or LSWI = 0). These low EVI2/LSWI values can serve as indicators of bare ground/soil signals, which can be identified by the EVI2/LSWI values associated with all troughs in each candidate cycle (Liu et al., 2020; Zhang et al., 2022). Therefore, a new condition known as the “bare soil rule” was proposed. This rule effectively tackles the commission of incorrectly identifying false cycles and peak in the overwintering period in the MCD12Q2 algorithm (Fig. 5 c, 6 a).

Low EVI2 referred to the EVI2 related to the right trough ($EVI2_{Right}$) was less than a specified EVI2 threshold ($EVI2_{thld}$). The $EVI2_{thld}$ was determined using Eq. (4), which takes into account various factors. The SWIR band is sensitive to both leaf water content and soil moisture. It is commonly utilized in the development of water-related vegetation indices such as LSWI (Xiao et al., 2002a; Xiao et al., 2002b). Green leaves havehigher NIR reflectance than SWIR reflectance, resulting in a positive LSWI value (>0). In contrast, senescent or dead leaves and soils have lower NIR reflectance than SWIR reflectance, leading to a negative LSWI value (<0). Consequently, the LSWI can be employed to identify the presence of bare soil at the end of a growing season (Zhang et al., 2022). This additional true peak criterion ($EVI2_{Right} < EVI2_{thld}$ or $LSWI_{Right} < 0$) becomes crucial when the amplitude ratio rule fails and is essential for the accurately identifying the periodicity in multi-season crops. It is important to note that the threshold of $LSWI_{Right} < 0$ is suitable for the majority of land cover types. Previous studies have demonstrated that the LSWI tends to be higher (usually not exceeding 0.2) in areas with high soil moisture (Liu et al., 2020). Although this threshold may not be met in wet soil conditions, the cycle/peak can still be identified usingother following parallel conditions (ConT2 or ConT3).

$$EVI2_{thld} = EVI2_{min} + (EVI2_{max} - EVI2_{min}) \times 0.15 \quad (4)$$

where $EVI2_{thld}$ is the EVI2 threshold, $EVI2_{min}$ and $EVI2_{max}$ are the minimum EVI2 and maximum EVI2, respectively.

True peak condition (2) (ConT2): If a cycle fails to satisfy ConT1 (amplitude ratio rule) but has an amplitude ratio (RA_{right}) lowerthan 35% and an $EVI2_{Right}$ lower than $EVI2_{thld}$ according to the bare soil rule, it is still possible for both the cycle and its corresponding peak/right trough to be considered true. This is contingent upon the fulfillment of

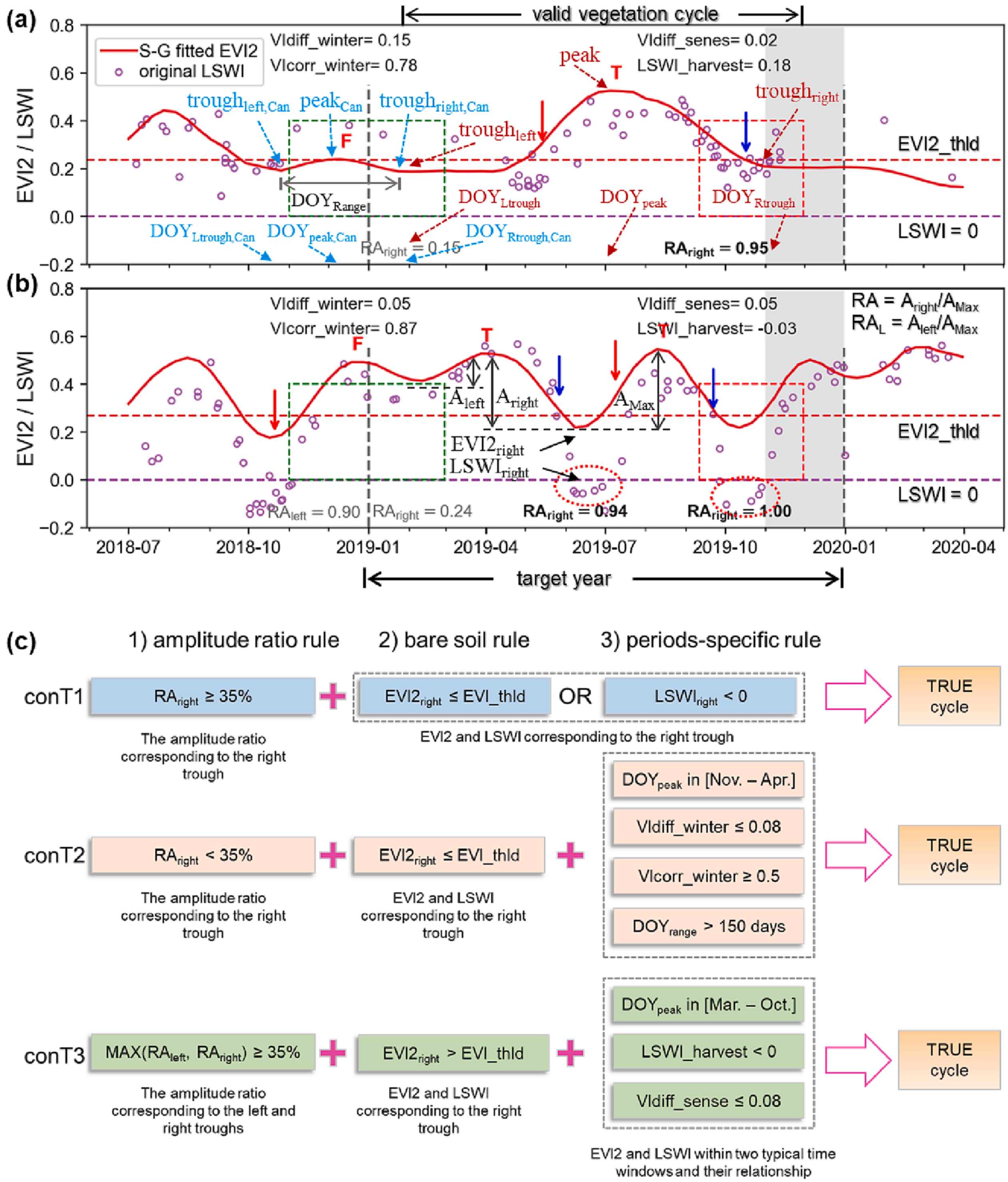

Fig. 5. Illustration of identification of valid cycle from combined Landsat/Sentinel vegetation indices (EVI2 and LSWI). The blue and purple hollow circles represent the original quality-control EVI2 and LSWI time series, and the red and orange curves represent the fitted EVI2 and LSWI curves, respectively. The horizontal blue and black dashed lines represent the EVI2 threshold and LSWI = 0 respectively, both of which are used to identify the bare soil, thus determining the true vegetation cycle. Red arrows represent SOS, while blue arrows represent EOS. The letter T denotes a real peak while F represents a false peak. The green dashed rectangle indicates the overwintering period (November of the previous year–February of the target year), while the red one indicates the senescence period (September-November of the target year). VIdiff_winter and VIcorr_winter denote the difference and correlation coefficient between EVI2 and LSWI time series during the overwintering period, respectively. VIdiff_senes denotes the difference between EVI2 and LSWI time series during the senescence. LSWI_harvest indicates the lowest value of LSWI during the vegetation harvesting or dormant period (gray shadow). A_{Max} denotes the maximum amplitude of all cycles in the target year. A_{Right} denotes the amplitude for the right trough related to a vegetation cycle. RA_{right} denotes the ratio (A_{Right}/A_{Max}) of A_{Right} to A_{Max} while RA_{left} denotes the ratio (A_{Left}/A_{Max}) of A_{Left} to A_{Max}. (For interpretation of the references to color in this figure legend, the reader is referred to the web version of this article.)

the following combination of sub-conditions (a-c).

A peak with an amplitude ratio (RA_{right}) of $\leq$ 35% does not necessarily indicate a false peak. This is particularly true for certain winter rapeseed crops (Fig. 6 e). The reasons for this can becomplex. One common factor is that the right trough of the fitted EVI2 curve may be stretched to a higher value due to fewer valid observations, resulting in a lower amplitude. However, the right trough is still a true trough. Additionally, in some regions like Hebei Province in China, winter wheat meets the first two conditions (amplitude ratio rule and bare soil rule) due to dry soil conditions, despite the presence of wheat growth during the overwintering period (Fig. 6 f, S1 c-f). After conducting numerous experiments, we have utilized the relationship between EVI2 and LSWI to effectively compensate for the omission of true peaks in algorithms similar to MCD12Q2.

a) The occurrence of the peak is expected during the overwintering period, which typically spans from between November of the preceding year toApril of the target year. This criterion specifically applies to certain overwintering vegetation types during their overwintering phase, such as winter rapeseed (Fig. 6 e, true peak) and winter wheat (Fig. 6 f, false peak).

b) The mean difference (referred to as VIdiff_winter) between the original EVI2 and LSWI time series, after applying QA-based quality control, during the overwintering period should be<0.08; and their correlation coefficient (referred to as VIcorr_winter) should be greater than or equal to 0.5 (Fig. 5 c, 6 e, f). These rules highlight the favorable performance of winter rapeseed in meeting these criteria compared to other vegetation types, including natural vegetation (Fig. 6 e, f).

c) The difference in time length (referred to as DOY_{Range}) between left trough ($trough_{left,Can}$) and right trough ($trough_{right,Can}$) of the current cycle should be >150 days (Fig. 5 c, 6 e, f). These conditions, namely b) and c) can eliminate false cycles related to winter wheat during the overwintering period. This is because the DOY_{Range} of winter wheat is typically <5 months, or the VIdiff_winter exceeds 0.08 and VIcorr is below 0.5.

All of three sub-conditions (a, b, c) must be satisfied for the determination of a true peak. These thresholds have been established based on a previous study (Liu et al., 2020) and our extensive experiments. These sub-conditions are primarily designed to capture the growth characteristics of winter rapeseed, which typically exhibits a low peak during the overwintering period (Fig. 6 e). These sub-conditions are primarily designed to capture the growth characteristics of winter rapeseed, which typically exhibits a low peak during the overwintering period.

True peak condition (3) (ConT3): If a cycle does not meet the criteria of ConT1 nor ConT2, but instead has an $EVI2_{Right}$ greater than $EVI2_{thld}$ and the max amplitude ratio (i.e., MAX(RA_{left}, RA_{right})) associated with the left ($trough_{left,Can}$) and right ($trough_{right,Can}$) troughs exceeding 35%, it is still possible for both the cycle and its peak/right trough to be considered true. This is the case as long as the following combination of sub-conditions (a-c) are satisfied.

The condition ConT3 primarily applies to various types of vegetation, including natural vegetation such as deciduous forest, grassland, and shrubs, as well as single-cropping crops like rice, and multiple-cropping crops like double-cropping rice. In practice, a peak with $EVI2_{Right}$ greater than or equal to $EVI2_{thld}$ during seasonal transition does not necessarily indicate a false peak (Figs. 5, 6 h). In certain multi-cropping systems, such as double-cropping rice in southern China, the seasonal transition from early rice to late rice can be relatively short. During this transition period, farmers typically face time constraints as they rush to harvest the early rice and prepare the fields for planting late rice. As a result, the satellite may have a limited timeframe to capture bare soil, leading to a relatively high EVI2 value ($EVI2_{Right} \geq EVI2_{thld}$) associated with the right trough of the vegetation cycle. Additionally, frequency cloud cover can impede the availability of high-quality observations, further complicating the accurate identification of the right trough in the vegetation cycle (Fig. 6 g, h, July 2019) (Liu et al., 2020). Alternatively, the summer EVI2 of natural vegetation, such as forests, can experience significant decreases a lot due to various factors like cloud cover or drought. This can result in the ratio being >35% (Fig. 6 i) or <35% (Fig. 6 j). Consequently, the conventional 35% amplitude ratio rule in the MCD12Q2 algorithm may fail in such cases (Fig. 6 i). In other words, the application of the ConT3 condition, which requires requires $EVI2_{Right} \geq EVI2_{thld}$, remains valid regardless of the amplitude ratio of theright trough in the vegetation cycle.

Following extensive experimentation, a novel combination known as ConT3 was derived by incorporating the original EVI2, and LSWI and their relationship. ConT3 effectively addresses the challenge of omitting the true peak during short harvesting and transplanting period in certain multiple cropping systems., Additionally, it resolves the issue of mistakenly identifying the decline in forest EVI2 during summer as a true peak.

a) The peak in vegetation should fall within the period between March and October of the target year. This criterion primarily applies to natural vegetation and multi-cropping systems that involve a harvesting-transplanting period.

b) The lowest value of the original LSWI (referred to asLSWI_harvest) after QA-based quality control, during the vegetation harvest and/or dormant period (November-December) should be below 0 (Fig. 5 c). This criterion effectively differentiates between multi-season crops (LSWI_harvest < 0; Fig. 6 g, h) and natural vegetation characterized bywet soil and warm temperature duringthe dormancy phase (LSWI_harvest > 0; Fig. 6 i). For instance, in the case of double-cropping rice, although the LSWI is likely to be above 0 during the seasonal transition period, it will decrease below 0 for approximately 1–2 months after the late rice harvest (Fig. 6 g, h). Conversely, forests in humid areas typically exhibit LSWI values > 0 in November and December (Fig. 6 i).

c) The mean difference (referred to as VIdiff_senes) between the original EVI2 and LSWI time series after QA-based quality control, during the senescence period (September-November) should be below 0.08 (Fig. 5 c). In addition to the LSWI_harvest < 0 condition, which applies to natural vegetation in arid/semi-arid areas, we introduce another criterion to effectively distinguish between multi-season crops (VIdiff_senes < 0.08; Fig. 6 g, h) and natural vegetation characterized by dry soil and warm temperature during the dormancy phase (VIdiff_senes > 0.08; Fig. 6 j). For instance, when analyzing the senescence period of double-cropping rice, a good correlation between EVI2 and LSWI is observed (Fig. 6 g, h). However, in the case of forests of arid area, the correlation between EVI2 and LSWI is considerablyweaker (Fig. 6 j).

(3) If none of the true peaks were identified in the target year according to the previously mentioned rules, then the highest peak in the target year was considered the true peak.

(4) In cases where the peak and troughs do not meet the aforementioned rules, they should be removed.

(5) If consecutive two peaks or troughs occur are observed, only the maximum peak or minimum trough is retained. By following the aforementioned procedures, all valid peaks accompanied by their corresponding troughs ($trough_{left}$ and $trough_{right}$) for the target year were successfully identified. The timing of the peak, $trough_{left}$ and $trough_{right}$ was labeled as DOY_{peak}, $DOY_{Ltrough}$, and $DOY_{Rtrough}$, respectively (Fig. 5 a, b).

2.4.2. Detection of LSP metrics (SOS, EOS, GSL, and POS)

In this study, a dynamic threshold-based method was employed to retrieve the phenological metrics for each valid cycle. The method involved calculating the ratio of EVI2 amplitude in the smoothed EVI2 time series. Based on this ratio, several key phenological metrics were retrieved, including the start of the growing season (SOS), the end of the growing season (EOS), the length of the growing season (GSL), and the peak growing season (POS). Additionally, the number of valid cycles was determined as part of the analysis (Bolton et al., 2020; Gray et al., 2019). All phenological metrics in this study depend on the $trough_{left}$, $trough_{right,}$ and peak of the valid cycles identified in Section 2.4.1.

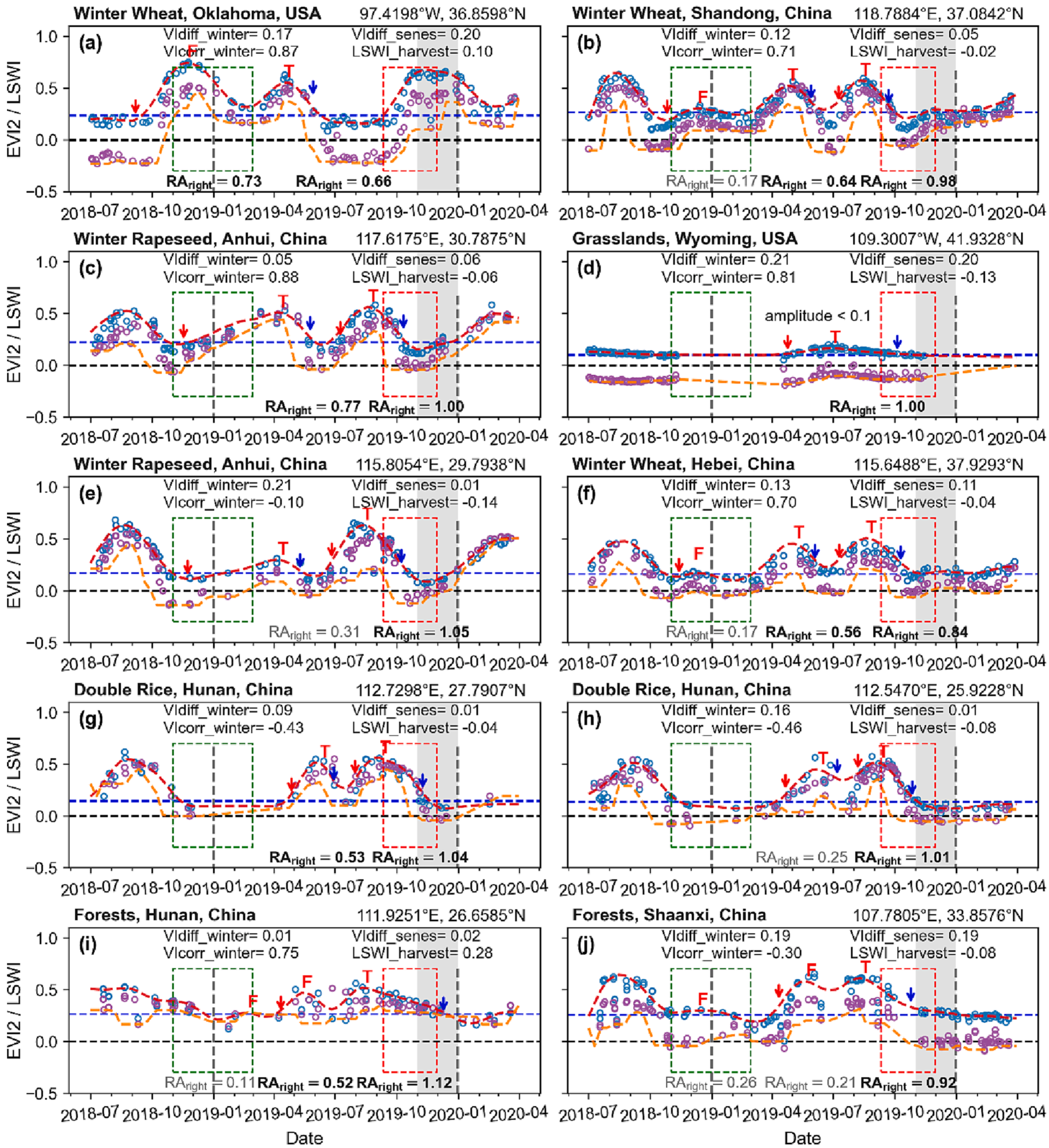

Fig. 6. Illustration of identification of the valid vegetation cycles by the temporal profile of vegetation indices (EVI2 and LSWI) from combined Landsat-Sentinel imagery covering the target year 2019 at ten sample sites. The cyan and purple hollow circles represent the original quality-control EVI2 and LSWI time series, and the red and orange curves represent the fitted EVI2 and LSWI curves, respectively. The horizontal blue and black dashed lines represent the EVI2 threshold and LSWI = 0 respectively, both of which are used to identify the bare soil, thus determining the true vegetation cycle. Red arrows represent SOS, while blue arrows represent EOS. The letter T denotes a real peak while F represents a false peak. The green dashed rectangle indicates the overwintering period (November of the previous year–February of the target year), while the red one indicates the senescence period (September-November of the target year). The gray vertical dotted line represents the range of the target year (e.g., 2019). VIdiff_winter and VIcorr_winter denote the difference and correlation coefficient between EVI2 and LSWI time series during the overwintering period, respectively. VIdiff_senes denotes the difference between EVI2 and LSWI time series during the senescence. LSWI_harvest indicates the lowest value of LSWI during the vegetation harvesting or dormant period (gray shadow). RA_{right} denotes the ratio of amplitude for the right trough to the maximum amplitude of all cycles in the target year. $RA_{right} \leq 35\%$ is marked in black, and $< 35\%$ is marked in gray. (For interpretation of the references to color in this figure legend, the reader is referred to the web version of this article.)

Specifically, we first updated the dates (DOYs) corresponding to the timing of $trough_{left}$ ($DOY_{Ltrough}$), $trough_{right}$ ($DOY_{Rtrough}$), and peak (DOY_{peak}) for all cycles one by one, respectively (Fig. 5 a, b, 6).

(1) For POS, the DOY_{peak} was sought as the date corresponding to the maximum EVI2 value between the $DOY_{Ltrough}$ and the minimum of $DOY_{Rtrough}$, or November 31st of the target year. The Subsequently, the POS was identified as the DOY_{peak} plus the mid-point of the window ($POS = DOY_{peak} + window\_size/2$) (Yang et al., 2019). The window_size means the size (9 days) of composition window.

Furthermore, we set threshold values on the green-up phase and green-down phase to estimate SOS and EOS dates, respectively. Since EOS was used for SOS extraction of overwintering vegetation, EOS was determined first and then SOS.

(2) For the EOS, the updated $DOY_{Rtrough}$ should be the minimum value between DOY_{peak} and $DOY_{Rtrough}$. To extract the EOS, apre-specified threshold of 15% was was applied during green-down phase. The EOS was identifiedas the first day (day of year, DOY) when the reconstructed daily EVI2 curve crossed this 15% threshold for each pixel in the target year (Bolton et al., 2020; Shen et al., 2014; Yang et al., 2022). Ultimately, the EOS was identified as EOS plus the mid-point of the window (EOS = EOS + window_size /2).

(3) For SOS, to ensure that the SOS of overwintering vegetation occurred in the preceding year, a strategy was proposed to dynamically update the threshold for extracting the SOS value. This approach aimed to avoid situations where a high threshold would cause the SOS to occur in the target year, which is not consistent with the definition of SOS as the start of the growing season, or leaf emergence. It's important to highlight that that the mismatch mentioned has not been effectively addressed by commonly used phenological algorithms, including MCD12Q2 and MSLSP30NA. These algorithms have not provided a satisfactory solution to the issue of inconsistent SOS retrieval, where some pixels indicate emergence dates (e.g., in autumn 2018) while others indicate green-up dates (e.g., in spring 2019) (Fig. S1). To ensure consistency and adherence to a unified definition,the retrieval of SOS should strictly adhere to the principle that SOS represents the emergence date of vegetation. Particularly for a large-region products, it is crucial to achieve a unified results of SOS, where all pixels consistently indicate the emergence of vegetation. After conducting numerous experiments, we discovered a simple and effective method to extract the SOS for overwintering vegetation. We observed that the EOS occurring before September of the target year served as a reliable indicator for extracting the SOS of overwintering vegetation. For overwintering vegetation in the Northern Hemisphere, the EOS typically occurs before June, while for natural vegetation, the EOS does not occur before September. By considering the duration of the vegetation cycle ($DOY_{range} > 90$ days), we can exclude false cycles that may occur during the overwintering period for natural vegetation. This ensures that the SOS of overwintering vegetation appears in the preceding year, irrespective of the amplitude ratio of the left trough (whether it is 15% or 50%). To provide flexibility and accommodate different scenarios, we relaxed the criteria and used the month of September as a reference point. The details were as follows.

a) If a cycle's $DOY_{Ltrough}$ was identified in the preceding year and its EOS occurred before September of the target year, and the duration of this cycle (DOY_{range}) was >90 days, the $DOY_{Ltrough}$ remained unchanged and wasnot updated. To extract the SOS, a threshold of 1% was set as the criterion (Fig. 5 a-b, 6 a, b, f). Identifying an EOS appeared before September allowed us to associate it with overwintering vegetation, where the SOS occurred in the winter. This approach ensured that the SOS of overwintering vegetation with relatively small growth amplitude (<15%) detected by remote sensing during the overwintering period would be attributed to the previous year (Fig. 6, S1).

b) If a cycle's $DOY_{Ltrough}$ was observed in the preceding year, and its EOS occurred after September of the target year, the $DOY_{Ltrough}$ needed to be adjusted. It was moved forward to the spring season and updated as the date corresponding to the minimum EVI2 value between $DOY_{Rtrough,Can}$ (the candidate $trough_{right,Can}$ that was closest to and later than the $DOY_{Ltrough}$) and DOY_{peak} (Fig. 5 a-b, 6 j). The threshold for identifying SOS was set at 15%. The presence of an EOS occurring after September indicated that the winter wave was associated with pseudo-fluctuations that were unrelated to actual vegetation growth.

c) If a cycle's $DOY_{Ltrough}$ was located in the target year, the updated $DOY_{Ltrough}$ was determined as follows. It was set as the date corresponding to the minimum EVI2 value between DOY_{peak} and the maximum value of either $DOY_{Ltrough}$ or DOY_{peak} minus a maximum green-up period length parameter (185 days) (Fig. 5 a-b, 6, S1). The threshold for identifying the SOS was set at 15%. The length parameter was referred on a previous study (Bolton et al., 2020). To calculate the final SOS, the last day (day of year, DOY) when the reconstructed daily EVI2 curve crossed above the pre-specified threshold during green-up phase was determined. The SOS was then adjusted byadding the mid-point of the window (i.e., SOS = SOS + window_size/ 2).

Moreover, to avoid misinterpretation caused by temporal fluctuations in the time series, only candidate SOS (EOS) dates that correspond to increasing (decreasing) trends should be regarded as the final SOS (EOS) dates. Additionally, cycles within the target year are retained if their POS dates fall within the range of January to November of the target year. Alternatively, if the POS dates fall between November of the preceding year to March of the target year, along with EOS dates within the target year (e.g., during harvesting phase for crops), it takes into account the patterns of overwintering vegetation.

Finally, a post-processing was conducted to eliminate anomalous results in the LSP mapping. This step involved a pixel-by-pixel neighborhood analysis. Each central (target) pixel was examined along with its neighborhood window of 3 × 3 pixels were determined. If the difference in phenological metrics (SOS, EOS, and POS) between the central pixel and the median of the eight surrounding pixels exceeded 60 days, the phenological metrics result of the central pixel was replaced by the median value, otherwise, the SOS/EOS result value was not changed. The GSL was calculated as the difference between EOS and SOS (EOS minus SOS).

2.5. Algorithm assessment

For the validation of our algorithm and the resulting LSP30CHN product, we adopted two schemes. One was to compare three phenology products at the site scale, and the other was to compare the spatial consistency and details with MODIS products at the pixel scale.

2.5.1. Validation using multiple sources of phenology data

To independently quantify the LSP detection capability, we evaluated the LSP30CHN-derived phenological metrics in two dimensions (spatial and temporal), against those from ground observation and PhenoCam, respectively. Specifically, we conducted the ground observation-based validation of the LSP30CHN metrics using multi-source in-situ data derived from the field-based PhenOBN phenological records in China and GCC-based PhenoCam phenology in North America (mostly in the United States). We compared our LSP30CHN product with the latest MODIS official phenology data product (MCD12Q2) against in situ phenological data (PhenOBN) for 2019 in China because only ground-based phenological data for 2019 is available in this study. The vegetation types involved include deciduous broadleaf forests (DBF), and croplands (winter wheat, summer maize, single rice, and double rice). To facilitate comparison between PhenOBN- and LSP30CHN-based results, the median value within 3 × 3 pixel windows surrounding each PhenOBN station was used to extract phenological metrics from LSP30CHN results. We also extracted phenological data for MCD12Q2 by PhenOBN sites. We retained only those phenological results for which all three data products were simultaneously valid for the validation.

As a complementary solution to site validation, we also compared our product with two phenology data products (MSPLSP30_NA, and MCD12Q2) against in situ phenological data (PhenoCam) for 2016–2018 in North America to assess our LSP30CHN product robustness and scalability. Only those phenological results that correspond to all three data products simultaneously valid were retained in the validation. The vegetation types involved include DBF, grasslands (GRA), croplands (CRO), and wetlands (WET). To facilitate comparison results between PhenoCam and three phenological products, the median values of phenological metrics within 30 m, 30 m, and 250 m buffers covering each PhenoCam site were extracted from LSP30CHN, MSPLSP30_NA, and MCD12Q2 results, respectively.

In addition to spatial validation, we further compared the interannual variations of phenological metrics over 2016–2021 between LSP30CHN and MCD12Q2 datasets for temporal validation by using six CERN sites at the site and regional scales (Fig. S6). Here we selected the coordinate locations of these sites to extract the results of all phenology data products. These sites are carried out under the CERN framework following uniform standards, and these locations were as spatially homogeneous as possible, to confirm the temporal consistency of our algorithm and MODIS products, as well as the robustness of our algorithm.

2.5.2. Comparison to MODIS phenology product (MCD12Q2) at pixel scale

To complement the in-situ phenological observations-based validation, we compared the LSP30CHN with the MCD12Q2 phenology product. The MODIS LSP product is thought to offer high-quality phenological dates on a homogeneous surface; however, in China, a significant proportion of the land surface is heterogeneous (Fig. S10), consisting of a mixture of multiple land cover types. We compared LSP30CHN results to corresponding values from the MCD12Q2 data product for 2019 across different purity gradients.

Specifically, to explore the scaling effect which would affect the comparison, we compared the degree of phenological differences between the MCD12Q2 and LSP30CHN data products at different cover proportions for land cover types. In this study, 30 m-LC data is aggregated to the spatial resolution of 500 m using the majority method. Since it is difficult for a pixel to distinguish the contribution of natural vegetation and croplands to the spectrum and thus phenological retrievals, we calculated the proportion of major land cover type (i.e., purity ratio) of all 30 m vegetated pixels within a 500 m pixel (hereafter 500 m-LC). Vegetated pixels include all forests, shrublands, grasslands, savannas, and croplands according to the 30 m-LC classification scheme (Zhang et al., 2021b). All 500 m pixels are then divided into 7 categories of purity ratio (i.e., 90–100% (pure pixels), 80–90%, 70–80%, 60–70%, 50–60%, 40–50%, 30–40%). For each purity ratio, we further generated 100,000 random sample points for natural vegetated and all vegetation types using a stratified sampling strategy for 500 m-LC pixels across China, respectively (Fig. S10). The category with a purity ratio of $< 30\%$ is not included in this study due to insufficient sample size.

The LSP30CHN was compared to the MCD12Q2 at a spatial scale of 1×1 MODIS pixels (Bolton et al., 2020), we also examined the comparison at the 3×3 MODIS pixels but not shown. To do this, the median values in 1×1 MODIS pixel windows for each phenological metric (SOS or EOS) were calculated from LSP30CHN and MCD12Q2 data. Following the application of land cover, MODIS pixels with $< 25\%$ coverage of LSP30CHN pixels were excluded from the analysis, along with MODIS pixels with QA scores of “fair” or “poor”. To rule out the possibility that variations in some specific samples caused the validation results, we repeated the analysis three times, each time generating 100,000 samples by random resampling across China.

In addition to the nationwide general comparison between two phenology products (LSP30CHN vs MCD12Q2) at the 30 m and 500 m scales, we also examined their differences in complex agricultural systems in two typical hotspots (see Fig. S11 for details), both of them were rectangles with a buffer of 25 km (Fig. S11): (1) the Sanjiang Plain in Northeast China with a mosaic distribution of three crop types (maize, soybean, and rice; region 1, Fig. S11 a-d) (You et al., 2021) and (2) the Changzhutan region in Hunan Province with multiple cropping intensities (single- and double-rice; region 2, Fig. S11 e-h) (He et al., 2021). We made time series of EVI2 for one 500 m MODIS pixel and three (for region 1) and two (for region 2) 30 m crop subclass pixels inside this MODIS pixel, respectively (single-pixel scale) for 2019 to compare the seasonal variances of the 30 m and 500 m data. On the other hand, we calculated frequency distributions of SOS and EOS dates of all 30 m and 500 m pixels in these two hotspot areas with a 25 km buffer (regional scale), respectively, to assess their performances in representing the spatial heterogeneity and seasonal distribution of complex phenological patterns.

3. Results

3.1. Spatial and temporal validation of the accuracy of the LSP30CHN data

We conducted the validation of leaf emergence (SOS) and senescence (EOS) dates of LSP30CHN and MODIS phenology data for China using in-situ phenological observations. As for deciduous broadleaf forests, the SOS of LSP30CHN is significantly correlated to in-situ observations with a coefficient of determination (R^2) of 0.86 and an RMSE of 8.41 days (Fig. 7 a). On the other hand, the EOS dates of LSP30CHN showed R^2 of 0.80 and RMSE of 10.77 days (Fig. 7 g). In terms of agricultural ecosystems, the LSP30CHN results of a large proportion of sites showed a close correspondence with in-situ observations, although slight bias occurred at most sites (i.e., LSP30CHN predicted earlier SOS and later EOS). As for SOS results, four crop types have similar validation accuracies except winter wheat has the lowest consistency (Fig. 7 b-f). Specifically, summer maize has the strongest relationship (Fig. 7 c, $R^2 = 0.82$, RMSE = 11.80 days) with in-situ observations, followed by early rice (Fig. 7 e, $R^2 = 0.78$, RMSE = 11.54 days), single rice (Fig. 7 d, $R^2 = 0.72$, RMSE = 8.68 days) and late rice (Fig. 7 f, $R^2 = 0.66$, RMSE = 10.54 days), while the relationship was weakest for winter wheat (Fig. 7 b, $R^2 = 0.37$, RMSE = 22.38 days) showing earlier SOS of LSP30CHN than ground observations. On the other hand, as for EOS results, winter wheat has the strongest relationship (Fig. 7 h, $R^2 = 0.73$, RMSE = 7.73 days), followed by late rice (Fig. 7 l, $R^2 = 0.66$, RMSE = 8.36 days), summer maize (Fig. 7 i, $R^2 = 0.63$, RMSE = 7.84 days) and single rice (Fig. 7 j, $R^2 = 0.65$, RMSE = 15.60 days), while the relationship was weakest for early rice (Fig. 7 k, $R^2 = 0.51$, RMSE = 10.04 days).

On the contrary, for all vegetation types, whether SOS or EOS, the MCD12Q2 product showed worse results. Specifically, the best results were obtained for broadleaf deciduous forests (Fig. 7 a, $R^2 = 0.57$, RMSE = 15.58 days for SOS, while Fig. 7 g, $R^2 = 0.51$, RMSE = 10.77 days for EOS), but this was still worse than LSP30CHN. For crops, the MCD12Q2 showed a greater span of estimated phenological metrics, which probably led to a low correlation coefficient. Three of the four types of crops had $R^2 < 0.1$ (Fig. 7), except for late rice, which had relatively high consistency (Fig. 7 f, $R^2 = 0.63$, RMSE = 10.54 days for SOS while Fig. 7 l, R2 = 0.15, RMSE = 27.45 days for EOS). However, only 13.6% (6 out of 44) of the late rice sites that participated in the validation were successfully retrieved by MCD12Q2. It should be noted that a slight negative bias on phenology occurred at most sites indicating an earlier remotely sensed phenology than in-situ observations (Fig. 7). This phenological discrepancy is likely attributed to the difference between remote sensing- and in-situ observations in the definition of phenology (Donnelly et al., 2022).

We also compared LSP30CHN results with MSPLSP30NA and MODIS phenology data for North America using PhenoCam data. Overall, both SOS (Fig. 8 a-e) and EOS (Fig. 8 f-j) results were better for the LSP30CHN compared to the MSPLSP30NA and MCD12Q2, and the validation results for EOS were worse than SOS for all three products. Specifically, LSP30CHN was superior to the other two products, except for SOS for grassland (Fig. 8 c) and EOS (Fig. 8 g) for the evergreen coniferous forest, where MSPLSP30NA had a higher agreement. For broadleaf deciduous forests, LSP30CHN was similar to but superior (with lower RMSE) to MSPLSP30NA and MCD12Q2 (Fig. 8 a, f), and for deciduous broadleaf forests EOS, MCD12Q2 had a very low spatial consistency of EOS (Fig. 8 f). For crops, the SOS of LSP30CHN had significantly higher R^2 (Fig. 8 d) while the EOS of the three products performed comparably (Fig. 8 j). For the phenological results of the evergreen needleleaf forest, the three products are all poor, and there is a very low consistency of EOS (Fig. 8 b, g).

Moreover, we evaluated SOS dates estimated from LSP30CHN against that from MCD12Q2 over time (2016–2021) using CERN sites at the site and regional scales. During the period 2016–2021, although there are slight differences in magnitude, the interannual variation and

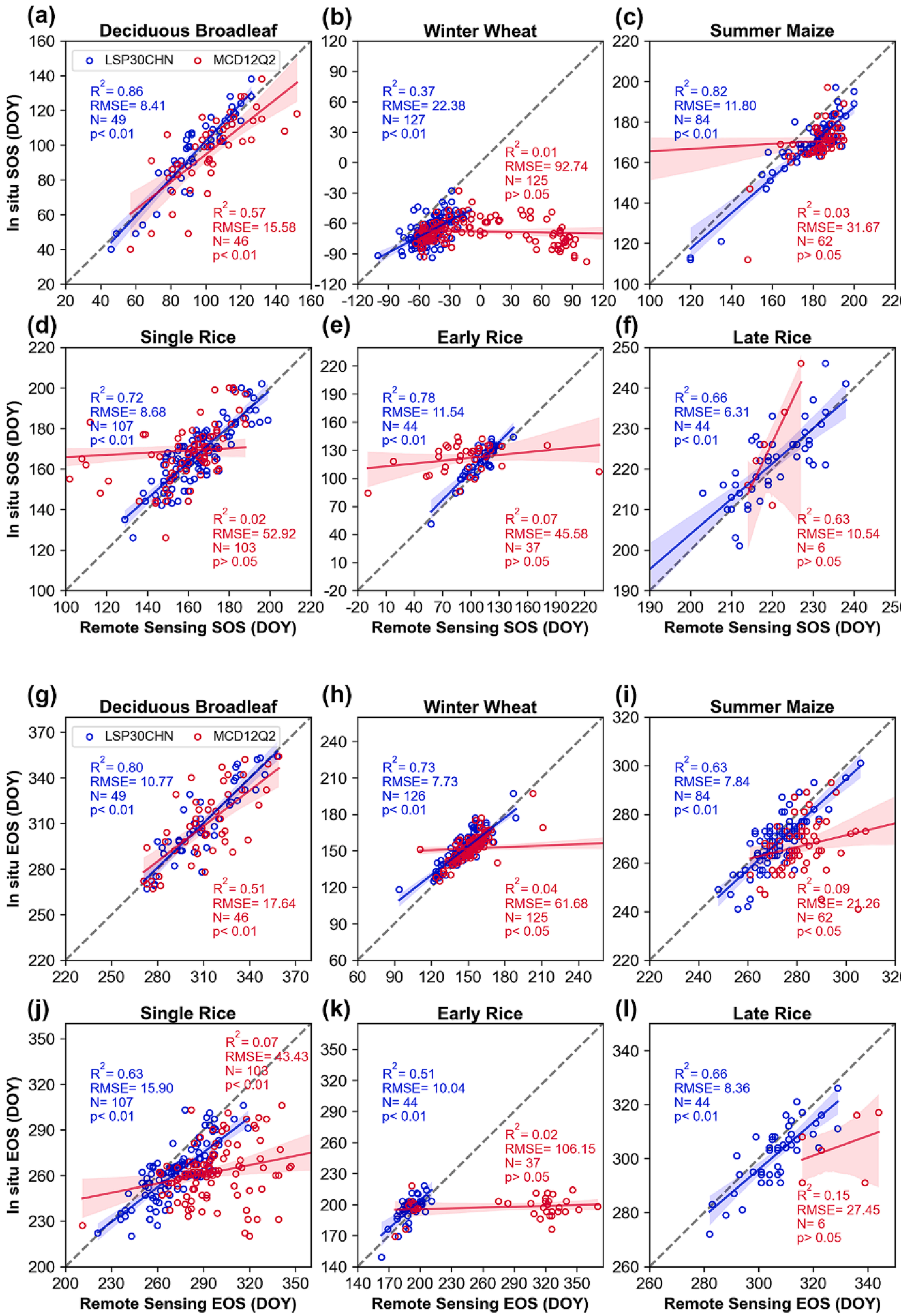

Fig. 7. The correspondence between LSP30CHN results and the in-situ phenological observations for SOS (a-f) and EOS (g-l) dates across six vegetation types. Here, early rice and late rice are distinguished, but both belong to double rice. A 1:1 line (gray dashed) is shown. Fitted linear regression and its 95% confidence intervals are also shown as solid lines and shaded areas for LSP30CHN (blue) and MCD12Q2 (red) products, respectively. (For interpretation of the references to color in this figure legend, the reader is referred to the web version of this article.)

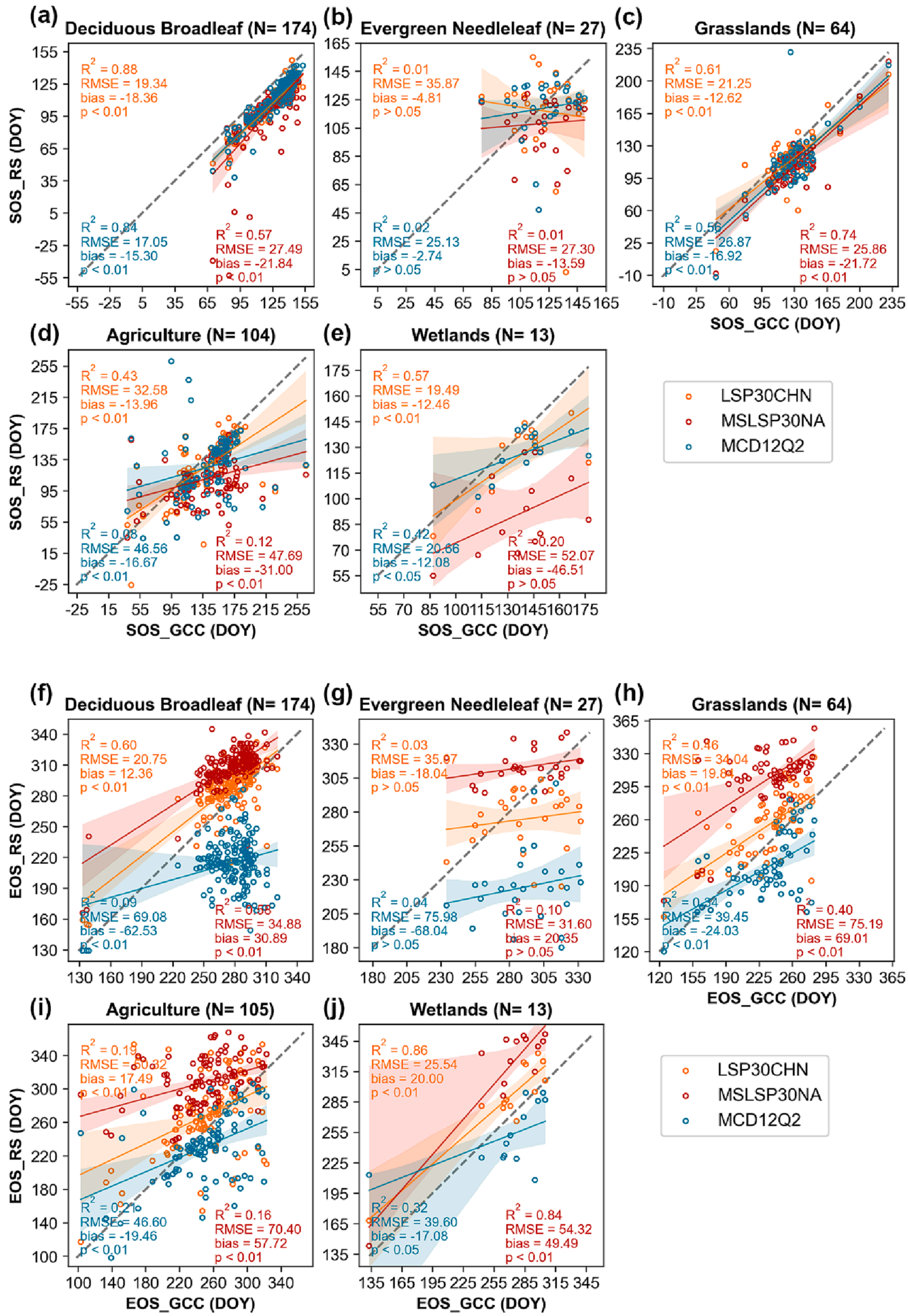

Fig. 8. The correspondence of SOS (a-e) and EOS (f-j) results between LSP30CHN and the other two phenology products against the PhenoCam observations across five vegetation types in North America. Orange, red, and cyan colors indicate LSP30CHN, MSLSP30NA, and MCD12Q2 products, respectively. The X-axis label represents the phenological results (SOS_GCC and EOS_GCC) simulated by PhenoCam, while the Y-axis label represents the phenological results (SOS_RS and EOS_RS) of the three products based on remote sensing. A 1:1 line (gray dashed) is shown. Fitted linear regression and its 95% confidence intervals are also shown as solid lines and shaded areas for three products, respectively. (For interpretation of the references to color in this figure legend, the reader is referred to the web version of this article.)

frequency distribution of SOS derived from LSP30CHN and MCD12Q2 were very consistent at the site scale (Fig. 9 a-f) and regional scale (Fig. 9 g-l), respectively. It is worth noting that LSP30CHN performed well in SOS of winter wheat while SOS of MCD12Q2 has large interannual variability, even SOS has a change of positive and negative sign (Fig. 9 d, j), which indicates that MCD12Q2 product has large uncertainties in extracting SOS of winter wheat.

3.2. Comparison of spatial consistency in scaling effects with the existing MODIS phenology data

In China, ~45% of vegetation pixels on a 500 m scale are considered pure pixels, and nearly 55% are mixed ones, with the proportion of mixed pixels ranging from 40 to 80% (Fig. S10). When only considering pure pixels (purity ratio = 10), the upscaled LSP30CHN phenological metrics showed good agreement ($r > 0.8$) with the MCD12Q2 product for both SOS (Fig. 10 a) and EOS (Fig. 10 i). It should be pointed out that the high scattering effect between these two products for both leaf emergence and fall senescence revealed modest systematic bias in MCD12Q2 phenological metrics versus results from the LSP30CHN algorithm. We found significant and consistent results occur with MCD12Q2 having later SOS but earlier-then-later EOS than LSP30CHN regardless of the pixel purity ratio (Fig. 10).

We further found that the heterogeneity gradient-induced scaling effect affects the spatial consistency of phenological retrievals between the LSP30CHN and MCD12Q2 products (Fig. 10). Specifically, the discrepancies in both SOS and EOS became larger as the purity ratio (higher values imply more homogenous surfaces) decreased from 90% to 40%,

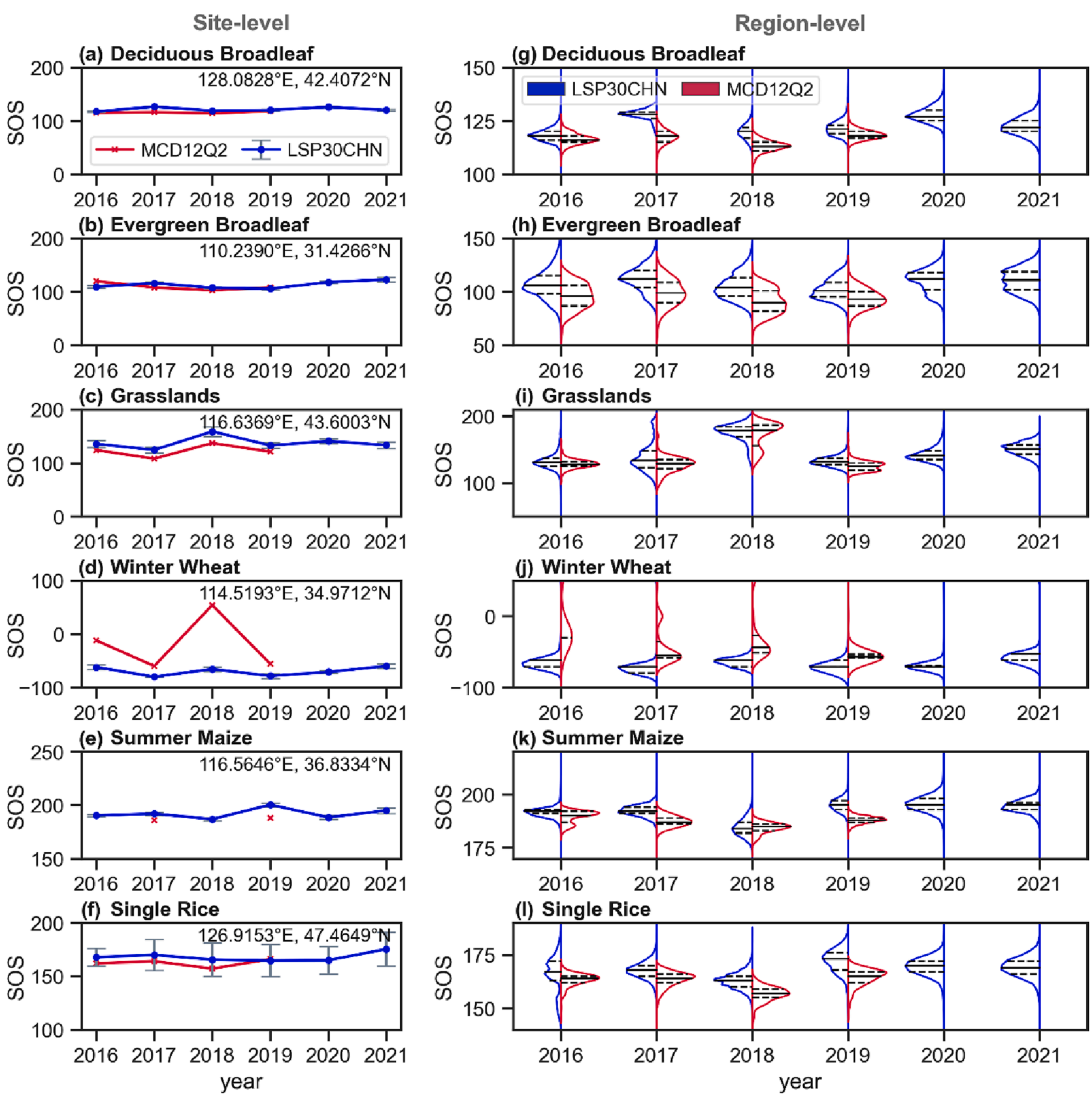

Fig. 9. Interannual variance (a-f) and frequency histogram distribution (g-l) of the start of the growing season (SOS) over 2016–2021 derived from LSP30CHN and MCD12Q2 among selected vegetation types. Blue and red colors indicate LSP30CHN and MCD12Q2 products, respectively. Site-level LSP30CHN-based SOS is the mean (±standard deviation) of all 30 m pixels within the corresponding 500 m pixels. The region-based frequency distribution for each site is obtained based on the SOS of all pixels (30 m LSP30CHN vs 500 m MCD12Q2) within a 25 km buffer around the CERN (Chinese Ecosystem Research Network) site. Dashed and solid lines in each violin are the 25% and 75% quantiles and the median values, respectively. Refer to Fig. S6 for more details. (For interpretation of the references to color in this figure legend, the reader is referred to the web version of this article.)

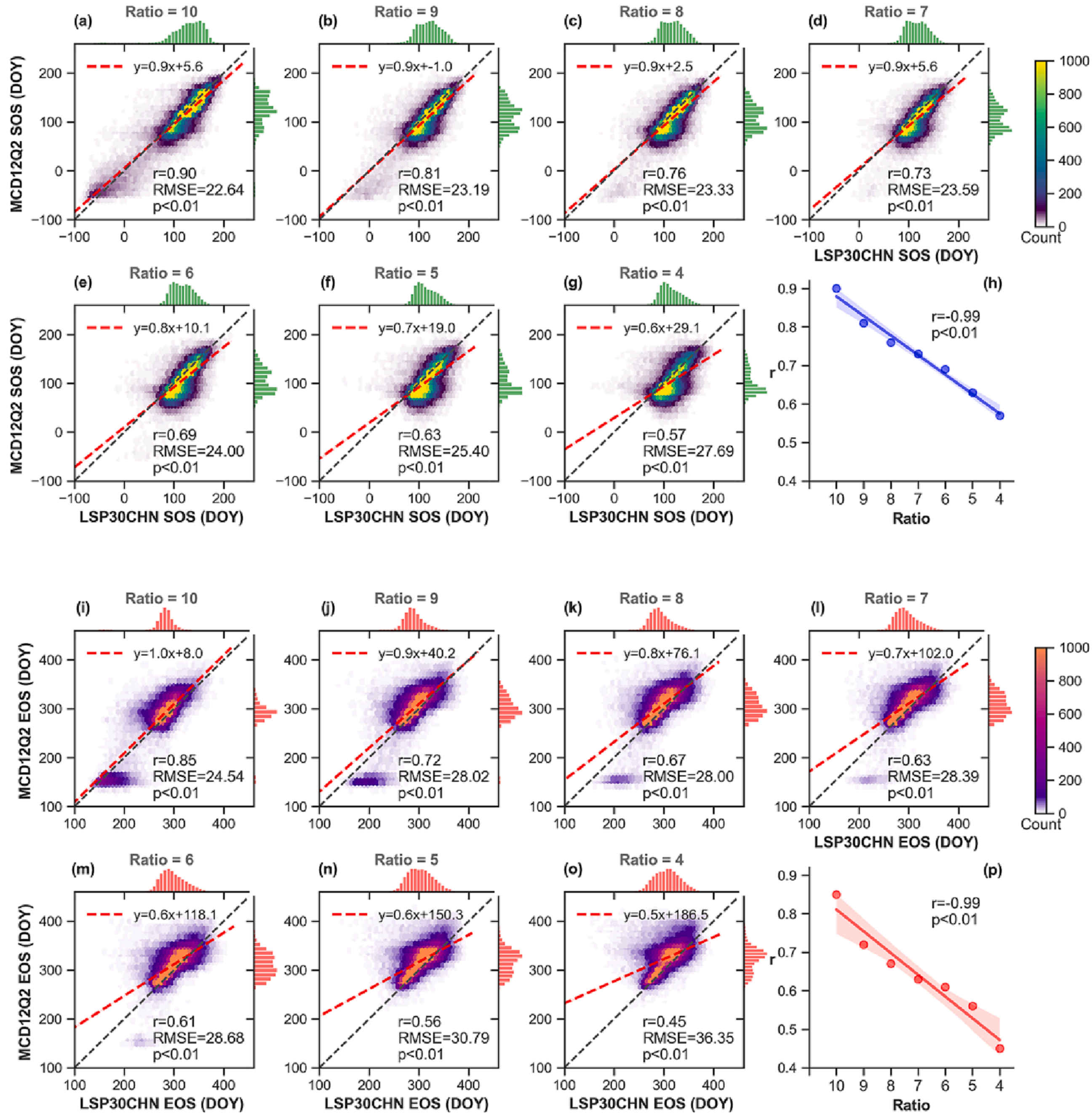

Fig. 10. The consistencies between LSP30CHN- and MCD12Q2-retrieved SOS (a-h) and EOS (i-p) for all vegetated 500 m pixels across different purity ratios, respectively. The purity ratio (Ratio #) indicates the proportions of 30 m major land cover type within a 500 m pixel corresponding MODIS pixel. For example, the Ratio = 10 represents the proportion between 90 and 100%. The Y-axis label in subplots (h, p) denotes Pearson's correlation coefficient between the two products.

and the differences showed a linear downward trend with *r* decreasing from 0.90 to 0.57 for SOS (Fig. 10 h) and from 0.85 to 0.45 for EOS (Fig. 10 p), respectively. We also only included natural vegetation for the comparison of LSP30CHN and MCD12Q2 across different purity ratios, and the result shows a consistent conclusion with that for all vegetation pixels (Fig. S12).

3.3. Spatial distribution of LSP30CHN-derived phenological metrics

The LSP30CHN data product showed a clear spatial pattern of phenological metrics and revealed finer spatial details (Fig. 11). Spatial patterns in the SOS, EOS, and POS showed substantial geographic variation related to climate forcing and land cover (Fig. 11 a-c). Specifically, a strong but heterogeneous latitudinal gradient in the leaf emergence (SOS) was evident, superimposed on regional patterns related to land use (e.g., croplands) and moisture limitations. For example, the growing season started later at higher latitudes. The SOS in the arid area of northwestern China was later than that in the humid area of southeastern China, consistent with the pattern of arid and humid zones in China (Fig. 11 a). In addition, impressively, the leaf emergence in the agricultural areas of Northeastern China (You et al., 2021) and the winter wheat (Dong et al., 2020) growing areas of Northern China appeared earlier than the surrounding natural vegetation (e.g. forests and grasslands), almost perfectly matching the spatial distribution of crops in these areas (Fig. 11 a). These similar characteristics were also consistently reflected in the EOS (Fig. 11 b) and POS dates (Fig. 11 c).

In addition, we found that two phenology datasets have a close spatial pattern (Fig. 12), but the comparison results at the regional scale

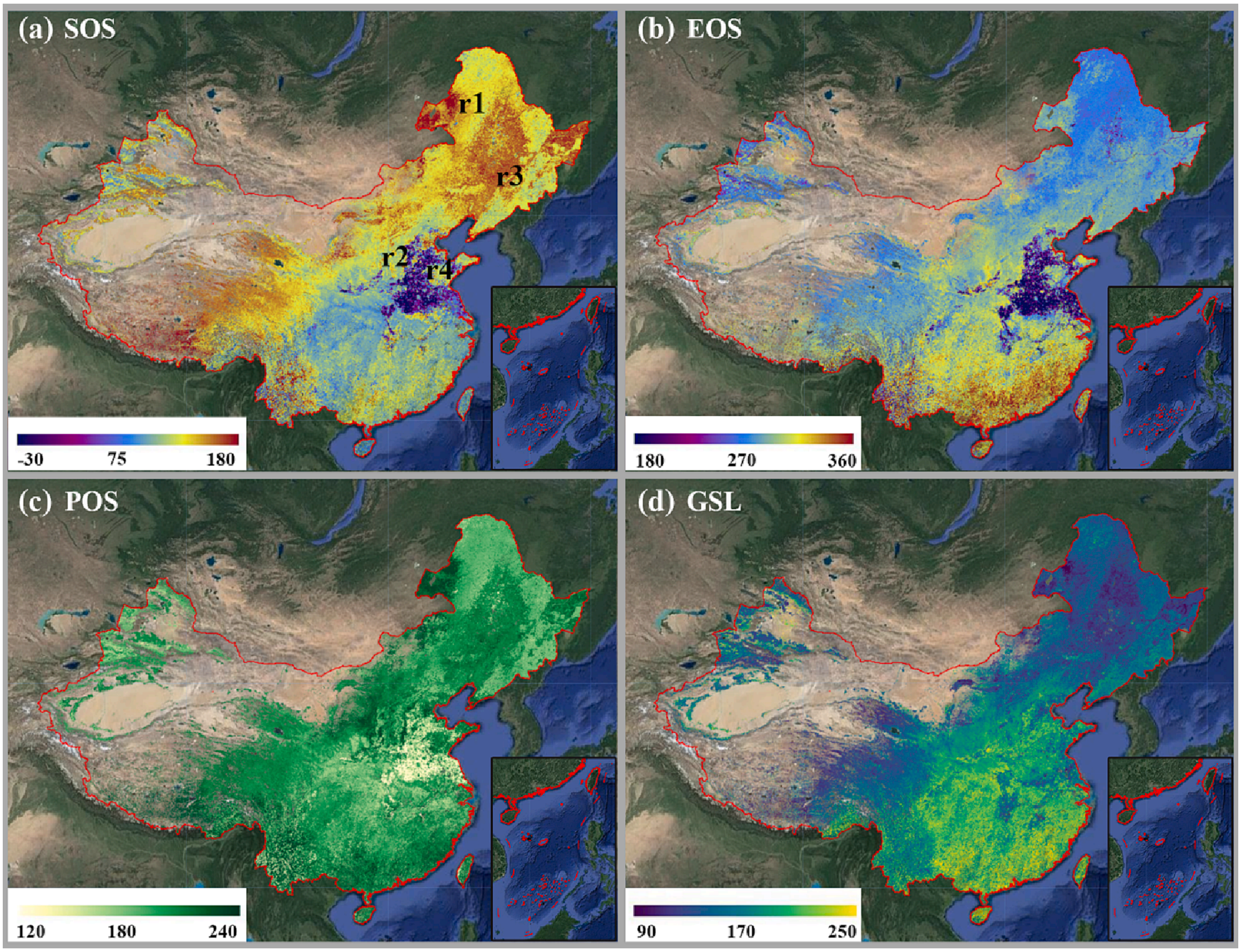

Fig. 11. Spatial distributions of the estimated (a) start (SOS), (b) end (EOS), (c) peak (POS), and (d) length (GSL) of growing season derived from LSP30CHN over China in 2019, respectively. The unit of the legend is day of year (DOY). The overlap map is Google Earth images.

demonstrated fine-scale phenology patterns captured by the 30 m EVI2 time series that are not captured by MODIS, particularly in locations with large spatial heterogeneity (Fig. 12). Fig. 12 a-c showed that field-to-field variability in crop phenology was also well captured by the LSP30CHN algorithm in the agro-pasture ecotone (agriculture and pasturage interlaced zone) of Inner Mongolia, which allowed crop phenology and greenness to be assessed across and within individual fields. The LSP30CHN provided more spatial details of vegetation phenology than the MCD12Q2 product. Fig. 12 d-f illustrated the spatial variability in SOS associated with land use patterns in a region of towns and suburbs located in Shanxi province. The vegetation SOS of cities/towns was exhibited in early spring (around May), and even the phenological details of street trees can be seen (Fig. 12 e-f). The SOS of the suburban farmland around towns appeared later (about June). On the contrary, the 500 m MCD12Q2 reflected shortened and blurred phenological differences in the city and surrounding farmland, and it is hard to distinguish cities and their boundaries from MCD12Q2 data. Fig. 12 g-i revealed elevation gradients with fine-scale spatial variation of deciduous forest-crop phenology related to land-use patterns in mountainous Northeast China. Earlier SOS in higher-elevation forests is evident, and the latter SOS is well-captured in lower-elevation croplands. Fig. 12 j-l showed the variable SOS dates of winter wheat associated with land use patterns in Shandong province. The phenological differences of crops with different growth patterns were well expressed by the LSP30CHN product, and winter wheat SOS was earlier. However, the MCD12Q2 product was not expressive enough in this respect. LSP30CHN showed a consistent pattern of SOS for winter wheat which occurred in the previous year (e.g., autumn–winter in 2018). On the contrary, it is worth noting that the SOS of some pixels, which is not negligible, obtained by the MCD12Q2 with a 15% threshold was positive (~90 DOY, Fig. 12 j) that means MCD12Q2-derived SOS occurred in the target year (e.g., in spring 2019). This issue may be caused by its phenology extraction algorithm mistakenly identifying the valid vegetation cycle between emergence and green-up date for winter wheat (Fig. 6 a, b, f, 12 j-l). This also demonstrated the robustness of LSP30CHN in delineating the complicated phenological pattern of land use and land cover. Comparisons of LSP30CHN results for all four cases with the MCD12Q2 product clearly illustrated that LSP30CHN results displayed a considerable degree of fine-scale spatial variation that cannot be captured in the MCD12Q2 dataset.

3.4. Performance of LSP30CHN in complex agricultural systems

We evaluated the potential of LSP30CHN in complex agricultural systems (Fig. 13). On the one hand, the spatial structure of crop mixing can be reflected in 30 m LSP30CHN in northeast China (Fig. S11 a-d). The 30 m LSP30CHN- and 500 m MCD43A4-based EVI2 time profiles were relatively similar in SOS but differed in EOS (Fig. 13). The MCD43A4 EVI2 signal was more dominated by maize-soybean mix information, while the EOS difference between maize and rice was about

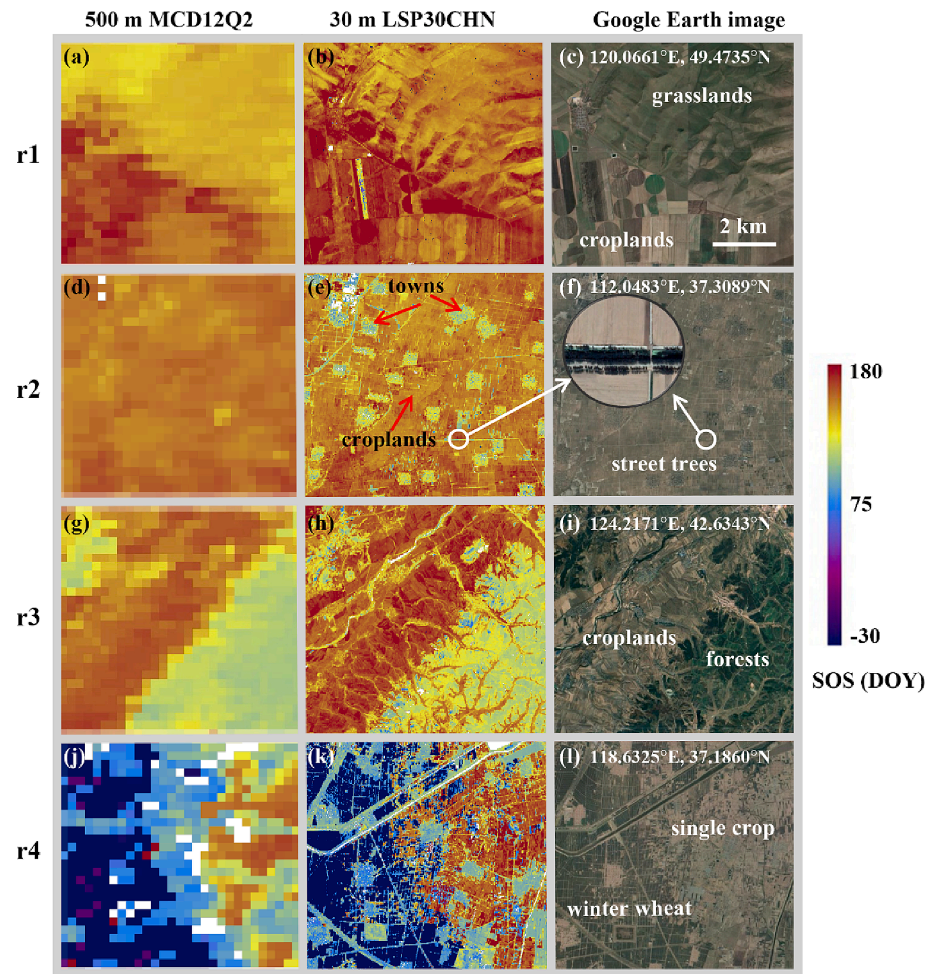

Fig. 12. Spatial comparisons of the start of the growing season (SOS) of the first vegetation cycle for LSP30CHN and MODIS C6 data products in 2019. Each row represents four different case analysis locations (r1-r4) that are highlighted in Fig. 11a, and include an agricultural-pastoral ecotone (a-c), a rural–urban mosaic (d-f), a crop-forest mosaic (g-i), and a winter wheat-growing area (j-l), respectively. Each column is 500 m SOS from the MCD12Q2 phenology product, 30 m SOS from LSP30CHN, and the Google Earth image of the zoomed area, respectively. Phenological metrics are shown as the day of year (DOY) with the same colormap as Fig. 11a. The center coordinates of these four regions are labeled in the third column.

20 days (Fig. 13 a). In addition, for the frequency histograms of the phenological metrics, the 30 m LSP30CHN reflected the distribution of crop types. The rice, maize, and soybean showed a misplaced frequency distribution (Fig. 13 c). The phenological dates of the three crop types, especially SOS, showed a strong overlap on the 500 m MCD12Q2. This meant that the 30 m LSP30CHN can distinguish the phenological dates of different crops. In comparison, the 500 m MCD12Q2, to some extent, cannot distinguish the phenological periods of various crops.

On the other hand, the 30 m LSP30CHN-based EVI2 time profile well matched the growth process of single- and double-season rice in Hunan province, but the 500 m MCD43A4 EVI2 curve only reflected the characteristics of a single growing season (Fig. 13 b, S10 e-h). The MCD43A4 EVI2 signal in green-up was more dominated by single rice information, although the EVI2 of senescence did not differ much between the two products (Fig. 13 b, d). In addition, for the frequency histograms of phenological dates, the 30 m LSP30CHN distinctly demonstrated the distribution of crop types with multiple growth peaks/cycles in SOS/EOS for single- and double-season rice (Fig. 13 d). On the contrary, the 500 m MCD43A4 product did not adequately capture the multi-peak phenological features for distinguishing single- and double-cropping rice, with only one peak distribution for both SOS and EOS.

4. Discussion

4.1. Advantages of the proposed uniform phenology algorithm

Although it is common sense that 30 m LSP data has better spatial characterization ability than 500 m LSP data, 30 m LSP data products at a global scale or continental scale are still very scarce so far (Bolton et al., 2020). The main limitation is that the complex seasonal characteristics (phenology) of different vegetation types make it difficult to develop a unified phenological extraction algorithm. Besides, the high-performance computing required for large-scale LSP estimations is becoming a major determinant. Therefore, the development of a 30 m large-scale LSP product closely related to these two constraints is still very worthwhile. Furthermore, given that the majority of phenological research has focused on North America and Europe, developing spatiotemporally explicit LSP data in China is imperative. Our algorithm could produce an LSP result regardless of the vegetation type of the target pixel (e.g., forest, grassland, single or multiple crops), and our results show that the phenology estimation is good. It should be noted that our LSP30CHN product developed for China have several improved characteristics that fit a big country with two typical features 1) higher spatial heterogeneity, and 2) multi-cropping systems. We aim at the shortcomings of the existing phenological algorithm and realize a robust and unified phenological algorithm based on parallel determination conditions for the first time. Our study not only fills the volume of global LSP data but also is the world's first implementation of a large-scale multi-year LSP product at a spatial resolution of 30 m embedded in the GEE.

On the one hand, the LSP community has made a lot of efforts for medium-resolution LSP retrievals, such as 10 m/30 m LSP data products at the national/continental scale mainly represented by Bolton et al. (2020) and Tian et al. (2021). However, these existing algorithms are quite insufficient to innovate a single algorithm for fast and accurate retrieval of phenological metrics across different vegetation types and to

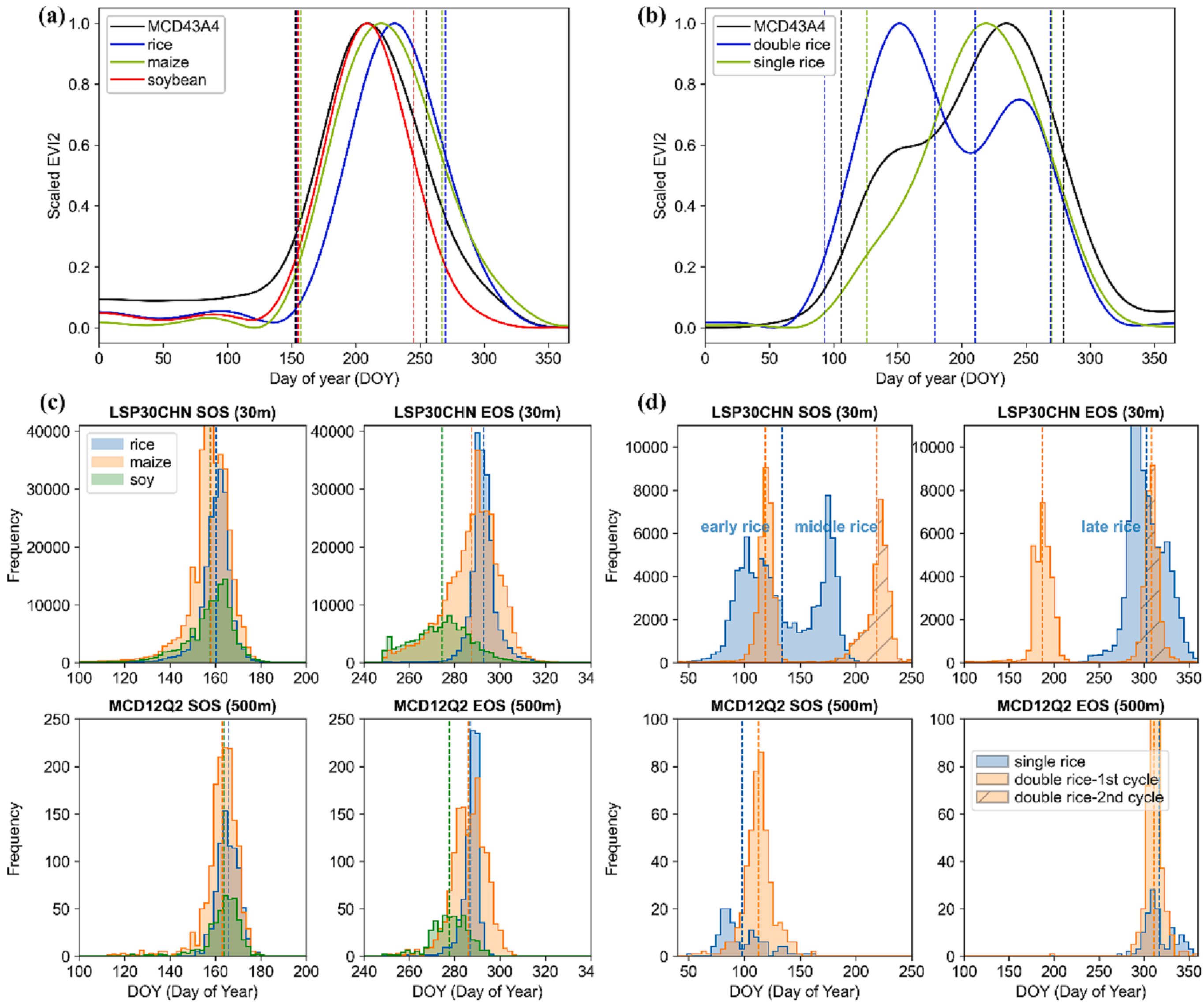

Fig. 13. Comparison of temporal profile (a, b) and frequency histogram (c, d) between 30 m (LSP30CHN) and 500 m (MCD12Q2) phenology products across different crop types. Two hotspot regions (see Fig. S11 for details), the Sanjiang Plain (a, c) and Changzhutan region in Hunan Province (b, d) were selected to illustrate the detailed differences between the two datasets in different land-use types. The EVI2 time series (a, b) of two selected 500 m MODIS pixels in the two above regions are shown, respectively. In a single 500 m MODIS pixel, there are multiple crop types or multi-cropping rice, which is indicated by many 30 m pixels. The vertical dashed lines in subplots (a, b) represent SOS and EOS, while the vertical dashed lines in subplots (c, d) indicate the average value of phenological metrics for each crop type.

obtain phenological metrics with unified definition and comparability. By using the EVI2 amplitude (>0.1) and amplitude ratio (>0.35) of the peaks, previous efforts of LSP retrieval usually tend to exclude the vegetation cycle during the overwintering period for the winter crops and/or the pixels of annual herbs with low amplitude in arid areas (Bolton et al., 2020; Gray et al., 2019; Qiu et al., 2020a). Here we argue that these phenological algorithms could not be used to identify accurate vegetation cycles in any ecosystem system (Figs. 6, 13, S1). We avoid the issue of mechanically masking dryland vegetation or evergreen plants that have too small a growth amplitude but still have seasonality in the existing phenology algorithms (this is the first shortcoming of the existing phenology algorithms). We also evaluated a separate rule for amplitude ratio > 35% in the existing phenology algorithms and found that this rule is not always competent for the determination of multiple growth cycles (this is the second shortcoming of the existing phenology algorithms). In general, these shortcomings exist in four complex cases as follows.

Case 1) For some winter wheat, a false peak with an amplitude ratio > 35% during the overwintering is mistakenly judged as true (Commission). This would lead to wrong retrievals of SOS or EOS (Fig. 6 a, S1 b). The EVI2 temporal profile of some vegetation to live through the winter, such as winter wheat in the North China Plain and the states of Oklahoma and Kansas in the United States, and winter rapeseed in southern China, usually has two peaks (late autumn and early spring) due to decreased EVI2 during the vernalization period in autumn and winter. These sometimes led to the minimum EVI2 amplitude being >0.1 and the amplitude ratio over 35% (Fig. 6 a, November 2018 to April 2019). In this case, such an operation (e.g., Bolton's method) could easily misidentify vegetation cycles, leading to an incorrect estimate of phenology. Specifically, for some winter wheat in the United States, if the amplitude ratio of EVI2 during the overwintering period is > 35%, the vegetation cycle during this period will be misjudged as the true cycle (Fig. 6 a). Also, only cycles with peaks appearing in the target year would be considered in the algorithm by Bolton et al. (2020); therefore, the SOS of winter wheat in Fig. 6 a, S1 b appeared in spring, which is obviously problematic. To say the least, even if the peak cannot be limited to the target year, then SOS may be correct, but this will still lead to EOS of winter wheat occurring in the winter or the preceding year or early spring of the target year, which is obviously problematic (Fig. 6 a, S1 b).

Case 2) For some winter rapeseed, a true cycle with an amplitude ratio < 35% during the overwintering is misidentified as false (Omission) (Fig. 6 e). Moreover, these two contradictory cases are often in the same period, and it is difficult to distinguish them by a single amplitude rule (>35%).

Case 3) For some double-season rice, a true peak with an amplitude ratio < 35% in summer is misidentified as false (Omission). (Fig. 6 h). The original method was specifically designed for single-season vegetation (e.g., natural vegetation and/or single-cropping systems), fewer attempts have been made both for single- and double-season croplands, especially for wheat-maize/rice and rice-rice rotation cropping systems (Qiu et al., 2020a). For example, as for double cropping rice in Southern China, the time gap between the early-rice harvesting and subsequent late-rice transplanting may be as short (e.g., within two weeks) (Fig. 6 g, h, July 2019) (Liu et al., 2020), and this is a widespread practice. Coupled with the possible insufficient valid satellite observations, the amplitude ratio at the rotation period will be < 35%, so it cannot be recognized as two cycles of double cropping rice (one for early rice and one for late rice) (Fig. 6 h).

Case 4) For some forests, a false peak with an amplitude ratio > 35% in summer is misidentified as true (Commission) (Fig. 6 i). For natural vegetation, due to interference such as cloud cover or drought, EVI2 sometimes decreases in some forests in summer. Depending on the situation, the ratio may be >35% (Fig. 6 i) or < 35% (Fig. 6 j), and the 35% amplitude ratio rule of the MCD12Q2 algorithm will fail. Not to mention the cases where EVI2 amplitude is often lower than 0.1 in arid areas and evergreen vegetation. Again, these two contradictory cases are often in the same period, and it is difficult to distinguish them by a single amplitude rule (>35%). When the above four cases are put together, the complexity makes it more difficult to conduct uniform phenological retrievals over large regions. This is the same problem in all current LSP products.

On the contrary, our study presents a unified algorithm for the powerful detection of LSP information with a spatial resolution of 30 m for different vegetation ecosystems, including natural and agricultural ecosystems (Fig. 5). The core of the algorithm is to extract accurate phenological metrics by refining the identification of a valid vegetation cycle (Figs. 5, 6). We used the original EVI2 and LSWI observations and their relationships within two key time windows, allowing for more accurate identification of the vegetation cycle (Fig. 5, and Section 2.4.1). Specifically, we innovatively developed two main determination conditions, one was to identify soil bare presence during the seasonal transition period, and the other was to use the vegetation indices and their relationships in a time window to assist in determining whether the target vegetation cycle (time window) was true or false. We found that the difference between EVI2 and LSWI of crops was small during the overwintering and senescence periods (Fig. 6). We also found that EVI2 and LSWI were very relevant during the overwintering period, and LSWI/or low EVI2 was largely able to monitor the bare soil presence during the senescence period (Fig. 6). This study identified the vegetation cycle based on the simple truth that bare soil and/or dead vegetation exists during the transition between two adjacent vegetation cycles. Both LSWI and low EVI2 could recognize bare soil during the temporal window of soil exposure in which the growing phase transforms (Xiao et al., 2006; Zhang et al., 2022), which also works for single-season forests and grasslands (Fig. 6 d, i, j). To date, we have not seen much work that ties LSWI-EVI2 and their relationships with accurate identification of phenological cycle. Through multi-level validation/comparison, our algorithm can identify more accurately the cycles of interannual crops and double-season crops with rapid seasonal transitions, such as winter wheat and double rice. Moreover, this idea of auxiliary time windows also alleviates the adverse effects of missing data to a certain extent. Our improved algorithm can be used for the phenological extraction of all vegetation types and can achieve the consistency of phenological results in the definition of phenological metrics, which can better meet the needs of scientific research and applications.

On the other hand, we pointed out and addressed the inconsistency of SOS extraction in the existing phenology algorithm, which has been always neglected. By definition, the SOS for overwintering vegetation, such as wither wheat, should be leaf emergence in the fall/winter of the previous year. As a large-region product, SOS results should be unified, instead of SOS with some pixels being emergence dates (e.g., in autumn 2018) while some pixels being green-up dates (e.g., in spring 2019). However, the extracted SOS for some winter wheat by the existing MCD12Q2-like algorithm will be highly variable across pixels in terms of the definition (Bolton et al., 2020). If the amplitude ratio of winter wheat during the overwintering period is below 35% (in many cases below 15%), the SOS timing extracted at a threshold of 15% or even 50% would cross over to the target year because it was misclassified as a green-up period, but in fact it should be the emergence date of the preceding year (Fig. 6 b, S1 c, e, f) (Bolton et al., 2020). And this issue could occur in the United States and a large number of winter wheat in the North China Plain (Fig. 6 b, S1 e-f). We argue that this issue is a big thing as this leads to inconsistency in the SOS results caused by the algorithm when applying or comparing phenological metrics among vegetation types at a large scale. We found the cause of this issue that makes SOS retrievals highly variable across pixels. For data-driven phenological retrievals, the identification of valid vegetation cycles determines the retrieval of phenological metrics (SOS and EOS). However, the rules of EVI2 amplitude (>0.1) and amplitude ratio (>35%) proposed by Bolton et al. (2020) cannot guarantee either the accurate identification of valid vegetation cycles or extraction of SOS/EOS in some cases.

Our algorithm ensured the consistency of SOS/EOS in the definition and retrieval results through the relationship between EVI2 and LSWI in the overwintering period (Fig. 6 a, b, f, and Section 2.4.2). In addition, we improved the criteria for determining the cycle corresponding to the target year. We switched from "simply considering the cycle in which the peak is located in the target year" to "considering the cycle in which the senescence or harvest time is in the target year, and considering the cycle in which the peak is before the winter of the target year" (Section 2.4.2). This ensured the determination of the true vegetation cycle of the overwintering crop (the peak may be in the previous year) and the following phenology extraction. Thus, our algorithm further reduced the uncertainty in the analysis of the temporal variation of the phenology. These improvements in our algorithm provide new insights into the large-scale refined phenological estimation for other regions with complicated, fragmented landscapes and vegetation seasonality. This is our big message and contribution to the community and science.

In addition, it should be noted that because a previous study showed that Bidirectional Reflectance Distribution Function (BRDF) correction did not have a significant effect on the phenology results (Tian et al., 2021), our study, therefore, did not apply BRDF correction to the remotely sensed data. In addition, although atmospheric correction and topographic correction are also factors affecting reflectance, given the complexity of these operations and the potential overcorrection of Sentinel-2 SR data on the GEE, we used TOA reflectance data, which also extends the study time span (2016–2021 for TOA while 2019–2021 for SR). Our study shows that although there is indeed a gap between TOA and SR in EVI2 magnitude, they are not very different for EVI2 phenology and even its interannual variance, especially in flat areas (Fig. S13).

4.2. Improvements of 30 m on 500 m LSP data

We implemented multi-level validation of our algorithm and product, including spatial and temporal validation, and comparison between multiple regions, types, and products. Our validation results with in-situ phenological observations are generally satisfactory ($R^2 > 0.6$ in most cases; Figs. 7-9). Our LSP30CHN product shows high comparability with the other two products (i.e., MCD12Q2 and MSLSP20NA) in terms of natural vegetation, and performs better than the other two products in most cases (Figs. 7-10). These evaluations demonstrate the high robustness and feasibility of our proposed LSP algorithm.

In addition to the advantages of accurate identification of valid vegetation and phenology extraction, a powerful strength of the LSP30CHN data is its capacity to characterize the phenological differences across land cover or climate zone at 30 m landscape scale, such as urban–rural difference, elevation gradient, and cropland/ natural vegetation mosaics, which are also affected by microclimate variation at a local scale (Gao and Zhang, 2021). Our study provided a quantitative phenological comparison between 30 m and vs 500 m- LSP data products at a national scale. The increasing inconsistency between LSP30CHN and MCD12Q2 LSP data products as the scaling effect increases revealed the latent scaling effects of coarser LSP products across China, which may affect the interpretation of biophysical properties of LSP (Fig. 10) (Peng et al., 2017; Zhang et al., 2017). The results demonstrate the potential necessity of 30 m LSP products in China and other regions with fragmented landscapes (Zhang et al., 2017). The new LSP30CHN allows us to realize the phenological identification and estimation of complex cropping systems and fragmented land-use patterns in China. The LSP30CHN product will enable the classification of cropping types, crop yield monitoring, and the evolution of cropping systems (e.g., crop rotation) for better supporting agricultural information management and food security at the sub-field level (Liu et al., 2020). This LSP30CHN will also support or re-examine the studies on urban ecology and health and sustainable management (e.g., urban green spaces) where the lack of vegetation dynamics characterized by satellite observations with high spatial and temporal resolution has previously limited assessments of urban ecosystems and its adaptation and mitigation actions (Li et al., 2019; Zhou, 2022). In addition, along with 500 m LSP data, the 30 m phenology data will allow for a much more detailed assessment of vegetation responses to disturbances, e.g., drought, flooding, insect infestations, and human influence, and for monitoring invasive species and vegetation diversity (Brooks et al., 2020; Pastick et al., 2020; Qiu et al., 2020b; Tian et al., 2021; Wang et al., 2018).

In addition, the cloud-based GEE platform facilitates the geospatial processing and analysis of large numbers of high-resolution and large-scale images for mapping vegetation phenology in a timely fashion. The approach of recursively identifying candidate cycles proposed by Bolton et al. (2020) is very hard to implement on the GEE because GEE operates on images rather than individual pixels. But our algorithm iterates over the peaks in the order they appear, making it easy to implement in GEE and other platforms. Therefore, our algorithm is simpler, easier to fit into the GEE platform, and easier to implement. It takes about 1.5 h to compute $\sim$ 7 tiles ($2^\circ \times 2^\circ$) in parallel from approximately 3 TB of imagery, and 326 tiles (Fig. S14) covering the whole of China will take about 4 days to complete. The occupancy of data storage for one year of data in China is $\sim$ 60G. Taking advantage of high-performance computing and parallel processing, our proposed phenology algorithm embedded in GEE can generate large-scale LSP products with fine spatial detail, and there will be invaluable insights and implications that the LSP community would address. The application of GEE allows us to produce 30 m or finer phenology data across a regional or global scale, and this capability further will be multiplied with Landsat 9 and PlaneScope data which can provide higher spatial and temporal resolution observations and can resolve the seasonal dynamics of vegetation at a finer spatial resolution than ever before (Masek et al., 2020; Zhao et al., 2022). Hence, in the future, the LSP30CHN data product is expected to have great potential for a broad range of new applications, such as agricultural policies (e.g., prediction of crop yields) (Zhang et al., 2019) and sustainable management (e.g., urban ecosystem health, urban green spaces, climate mitigation, and adaptation) (Vitasse et al., 2022) from local to the globe (Bolton et al., 2020).

4.3. Uncertainty analyses and implications for future work

The validation results show a satisfactory agreement with in-situ phenological observations, however, evaluation and validation of LSP data products still face several challenges that introduce uncertainty into the validation effort and should be improved in the future. First, the near-surface phenological observations are the sole touchstone and standard for developing and validating LSP algorithms and products. However, systematic and thorough comparable in-situ phenology measurements in China are mostly unavailable, and thus it is difficult to directly compare LSP metrics and their interannual variances retrieved from satellite-derived VIs with ground observations (Richardson et al., 2018a; Seyednasrollah et al., 2019a). That suggests a need for open and free access to phenological observations of longer duration and higher quality (Li et al., 2021). At the same time, we call for more observation networks (either based on repeated digital photographs or manual inspection) to join together to form a unified observing alliance, which will greatly standardize the patterns of observation, data management, and distribution. For example, increasing ground- and tower-based near-surface phenological observations would provide more measurements at the local scale, such as the National Phenology Network (USA-NPN, https://phenocam.sr.unh.edu/webcam) and the PhenoCam Network (Richardson et al., 2018b; Seyednasrollah et al., 2019a). A

Second, although the footprints are close, near-surface phenological observations (e.g., PhenoCam) and the 30 m landscape-based LSP still differ in the definition of vegetation phenology (Gao and Zhang, 2021; Melaas et al., 2016; Zhang et al., 2020b) as well as the scales (Peng et al., 2017; Zhang et al., 2017). Higher agreement between the LSP30CHN product and in-situ phenological observations was found in deciduous plant functional types (e.g., deciduous forests, grasslands) than in areas with lower seasonality in vegetation, such as evergreen ecosystems (Fig. 8 b, g) or arid and semi-arid systems (Fig. 6 d). The uncertainty in LSP30CHN data is attributed to its algorithm which is, by definition, designed to capture seasonal phenology in vegetation indices. Optical remote sensing to monitor the phenology of evergreen ecosystems remains a challenge. Although the criteria of the EVI2 amplitude greater than the prescribed threshold of 0.1 (i.e., $\Delta EVI2 > 0.1$) in the MCD12Q2-like algorithm has been abandoned in LSP30CHN algorithm, the interpretation of retrieved phenological metrics is ambiguous due to temporal changes from understory in open forests or overstory deciduous broadleaf trees in closed forests (Bolton et al., 2020). It must be acknowledged that it is challenging for all natural vegetation and crop SOS to be accurately extracted in one algorithm. We designed an effective way to extract the SOS of overwintering vegetation by identifying the false peak and true peak using the EOS of the cycle before September of the target year (Figs. 5, 6). While this still has potential impact of weeds on the algorithm's performance. For instance, in Fig. 6 b, the false peak may be caused by weed growth rather than the crop species. In some regions of southern China, where the climate is milder, it is possible for weed to continue growing throughout the winter season. This raises the challenge to distinguish between the peak caused by weed and the peak caused by the crop species. If the peak is caused by weed growth, the SOS may be estimated too early.

In this study, we found that LSWI or low EVI2 is successfully used for identifying the bare soil that indicates the end of the vegetation cycle, and then identified a complete valid vegetation cycle (Figs. 5, 6). Besides, LSWI and EVI2 time series have a good correlation between senescence and overwintering for the crop (Fig. 6). These biophysical characteristics of specific vegetation types found in this study and the amplitude criteria of previous studies (Bolton et al., 2020) are integrated into our algorithm, which can comprehensively and robustly identify the valid life cycle of any vegetation type and its critical phenological transition time (Figs. 5, 6). However, the optical satellite-based VIs values can still be affected by atmospheric conditions. We demonstrate for the first time that using the relationship between multiple vegetation indices at one stage of the vegetation cycle contributes to the identification of phenological metrics at other stages of the vegetation cycle and that this strategy can be effectively applied to time series with few or unavailable data observations.

Compared to Landsat-7/8, the Sentinel-2 sensor occupies the largest number of remote sensing observations, accounting for >60% of all valid observations (Figs. 2, 4). Multi-source data fusion can guarantee a valid observation every month for the implementation of the phenological algorithm (Fig. 2). Our results revealed that the 9-day composited Landsat and Sentinel-2 synthesis could detect the timing of emergence and senescence dates for most fields (e.g., cycles of cropland) but with some missing and false detections in Tibetan Plateau and the Sichuan Basin (Fig. 2). Harmonization is widely used in remote sensing, but rarely discusses its implications in downstream applications of spatial studies and especially for temporal studies. Although we reduced the impact of the bad quality of VIs time series by using the quality control, filter, and smoothing methods, some residual noise and abnormally low EVI2 values due to some failure detection of clouds (Fig. 4). In particular, bad-quality Sentinel-2 data in the peak season still cannot be ignored that inevitably affects the POS retrieval. To reduce such uncertainties, we harmonized the data from these three sensors and constructed 9-day maximum value composite (MVC) time series composites through gap-filling and data smoothing (see Section 2.3). The MVC can also be used to reduce the EVI2 mismatch of different sensors that may be caused by multiple factors (Figs. 4, S7, S8). In addition to data preprocessing, we also excluded those cases in which EVI2 decreased too much but was a single season through the above determination conditions of the true vegetation cycle (Fig. 6 i, j, Section 2.4.1) in the process of phenology extraction. These procedures could further to a certain degree reduce the impact of bad-quality of VIs on phenological retrievals. It should be noted that the Landsat-Sentinel-2 harmonization data has been well demonstrated for phenological retrieval of different natural vegetation and crops in the coastal zone (Zhang et al., 2022) and croplands (Liu et al., 2020) of China, and our study. Therefore, the harmonization scheme derived from other studies can be applied in this study with a great deal of confidence.

Our study shows that bare soil identification shows a great role in the identification of phenological cycle; however, although we integrate Landsat and Sentinel-2, bare soil identification based on optical remote sensing still faces great challenges in cloudy and rainy times and regions (Fig. 6 g, h). The identification of bare soil presence during periods of high cloud cover can be further improved by integrating optical and microwave sensors (e.g., Sentinel-1C-band synthetic aperture radar) and machine learning algorithms (Gao et al., 2021; Meraner et al., 2020; Meroni et al., 2021; Nasrallah et al., 2019; Salinero-Delgado et al., 2021). For example, both Sentinel-1 and Sentinel-2 can provide relevant and at times complementary LSP information at the field level, which is the frontier of science (Meroni et al., 2021). Whether and to what extent these two different monitoring approaches (optical and microwave) can achieve collaborative phenological retrieval is still unclear so far and needs further systematically exploited (Meroni et al., 2021). At present, there are more and more multi-source and multi-scale satellite cooperative observations. More recently, Landsat-9 (a virtual twin of Landsat-8) launched in September 2021, and the PlanetScope constellation of Dove CubeSat satellites affiliated with Planet Lab has been implemented since 2009. The medium-resolution Landsat and Sentinel-2 virtual constellation can provide more continuous global high-frequency satellite observations (every 1–2 days), which will be expected to provide considerable improvements to our algorithm, even to finer-resolution (e.g., ≤10 m) LSP retrieval (Tian et al., 2021). In the future, Sentinel-2C (3rd flight unit of the Copernicus Sentinel-2 mission) will be scheduled for 2023, and the Landsat Next mission (a constellation of three superspectral satellites in continuation of the Landsat series), is planned to launch by late 2030 and will provide enhancements to Landsat by providing more frequent observations, higher resolution images, and more than twice the spectral bands as its predecessors. It is also worth noting that commercial satellite programs with a high spatial (3 m) and temporal (daily) resolution, such as the PlanetScope satellite constellation, have been successfully used to monitor phenology at species and community scales (Cheng et al., 2020; Wang et al., 2023; Zhao et al., 2022), even in tropical forests (Wang et al., 2023). The PlanetScope data can achieve fine characterization of phenology with high spatial and temporal resolution from the individual–population–community–landscape scale, which was considered to bridge the scale gap between field measurements and satellite data observations from Landsat/Sentinel-2. The combination of Landsat/Sentinel and PlanetScope, therefore, is expected to solve the issue of scaling effects involved in land surface phenology related to climate change and anthropogenic impacts. These efforts will help simplify our phenology algorithms and enable a more robust algorithm on a global scale.

5. Conclusions

The generation of 30 m land surface phenology (LSP) for China is challenging due to the complex landscapes and diverse cropping systems. This study proposed a new robust and unified LSP algorithm by integrating all the available Landsat-7/8 and Sentinel-2 data on the Google Earth Engine. The core of our algorithm is to use the EVI2, LSWI, and their relationship to robustly identify individual valid vegetation cycles before a unified LSP retrieval. Our algorithm is suitable for most vegetation types, such as forests, shrublands, grasslands, crops, etc. The algorithm solves the problem of phenology extraction of overwintering crops such as winter wheat and multi-seasonal crops such as double-cropping rice with higher accuracy. Our LSP product (LSP30CHN) achieved satisfactory accuracy based on multi-source in-situ phenological observations. Moreover, the LSP30CHN product illustrates more detailed spatial and temporal information than the MCD12Q2 product. This study provides an advanced GEE platform-based LSP study case under different scenarios at landscape levels and provides technical support and application demonstration for field-level research such as crop management and land change monitoring. It is necessary to carry out more validation and algorithm improvement on a larger scale and more vegetation subtypes. Probably the biggest obstacle currently preventing the expansion of the algorithm to the global level is the lack of valid satellite observations, which makes it the existing gap-filling methods difficult to accurately reconstruct the original seasonal trajectory. Leveraging more remote sensing data with high spatial and temporal resolution (e.g., Landsat-9, Sentinel-1, and PlanetScope, etc.), our algorithm and product are expected to be applied to landscape-scale processes related to land cover, land use, and ecosystem function and change and to be extended from national/10-day level to larger spatiotemporal scales (continental and global scales) and at shorter temporal intervals (daily and 3–5 days).

CRediT authorship contribution statement

Jilin Yang: Visualization, Software, Conceptualization, Methodology, Validation, Formal analysis, Resources, Writing – original draft, Writing – review & editing. **Jinwei Dong:** Conceptualization, Validation, Writing – original draft, Supervision, Writing – review & editing, Project administration, Funding acquisition. **Luo Liu:** Methodology, Software, Writing – review & editing. **Miaomiao Zhao:** Writing – review & editing, Writing – original draft, Software, Methodology. **Xiaoyang Zhang:** Writing – review & editing. **Xuecao Li:** Writing – review & editing. **Junhu Dai:** Investigation, Writing – review & editing. **Huanjiong Wang:** Resources, Writing – review & editing. **Chaoyang Wu:**

Validation, Writing – review & editing. **Nanshan You:** Validation, Writing – review & editing. **Shibo Fang:** Resources, Writing – review & editing. **Yong Pang:** Resources, Writing – review & editing. **Yingli He:** Validation, Writing – review & editing. **Guosong Zhao:** Writing – review & editing. **Xiangming Xiao:** Validation, Data curation, Writing – review & editing. **Quansheng Ge:** Investigation, Writing – review & editing.

Declaration of Competing Interest

The authors declare that they have no known competing financial interests or personal relationships that could have appeared to influence the work reported in this paper.

Acknowledgments

This research was funded by the National Key Research and Development Program of China (2018YFA0606101), the Strategic Priority Research Program (XDA2601020201) of the Chinese Academy of Sciences (CAS), the National Natural Science Foundation of China (42201405) and China Postdoctoral Science Foundation (2022M713120). We thank the Google team for their excellent work on developing and sharing the Earth Engine platform (https://earthengine.google.com). We gratefully acknowledge the MODIS Science Team for generating and sharing various MODIS data (https://e4ftl01.cr.usgs.gov).

Appendix A. Supplementary material

Supplementary data to this article can be found online at https://doi.org/10.1016/j.isprsjprs.2023.07.017.

References

Arvidson, T., Goward, S., Gasch, J., Williams, D., 2006. Landsat-7 long-term acquisition plan. Photogramm. Eng. Remote Sens. 72, 1137–1146.
Bolton, D.K., Gray, J.M., Melaas, E.K., Moon, M., Eklundh, L., Friedl, M.A., 2020. Continental-scale land surface phenology from harmonized Landsat 8 and Sentinel-2 imagery. Remote Sens. Environ. 240, 111685.
Brooks, B.-G.-J., Lee, D.C., Pomara, L.Y., Hargrove, W.W., 2020. Monitoring broadscale vegetational diversity and change across north american landscapes using land surface phenology. Forests 11.
Chen, J.M., 2021. Carbon neutrality: toward a sustainable future. Innovation (N Y) 2, 100127.
Chen, J., Jönsson, P., Tamura, M., Gu, Z., Matsushita, B., Eklundh, L., 2004. A simple method for reconstructing a high-quality NDVI time-series data set based on the Savitzky-Golay filter. Remote Sens. Environ. 91, 332–344.
Chen, J., Zhu, X., Vogelmann, J.E., Gao, F., Jin, S., 2011. A simple and effective method for filling gaps in Landsat ETM+ SLC-off images. Remote Sens. Environ. 115, 1053–1064.
Cheng, Y., Vrieling, A., Fava, F., Meroni, M., Marshall, M., Gachoki, S., 2020. Phenology of short vegetation cycles in a Kenyan rangeland from PlanetScope and Sentinel-2. Remote Sensing of Environment 248.
Claverie, M., Ju, J., Masek, J.G., Dungan, J.L., Vermote, E.F., Roger, J.-C., Skakun, S.V., Justice, C., 2018. The Harmonized Landsat and Sentinel-2 surface reflectance data set. Remote Sens. Environ. 219, 145–161.
Copernicus, 2020. https://land.copernicus.eu/pan-european/biophysical-parameters/high-resolution-vegetation-phenology-and-productivity.
d'Andrimont, R., Taymans, M., Lemoine, G., Ceglar, A., Yordanov, M., van der Velde, M., 2020. Detecting flowering phenology in oil seed rape parcels with Sentinel-1 and-2 time series. Remote Sensing of Environment 239.
Descals, A., Verger, A., Yin, G., Penuelas, J., 2021. A threshold method for robust and fast estimation of land-surface phenology using google earth engine. Ieee J-Stars 14, 601–606.
Dong, J., Xiao, X., Menarguez, M.A., Zhang, G., Qin, Y., Thau, D., Biradar, C., Moore 3rd, B., 2016. Mapping paddy rice planting area in northeastern Asia with Landsat 8 images, phenology-based algorithm and Google Earth Engine. Remote Sens Environ 185, 142–154.
Dong, J., Fu, Y., Wang, J., Tian, H., Fu, S., Niu, Z., Han, W., Zheng, Y., Huang, J., Yuan, W., 2020. Early-season mapping of winter wheat in China based on Landsat and Sentinel images. Earth Syst Sci Data 12, 3081–3095.
Donnelly, A., Yu, R., Jones, K., Belitz, M., Li, B., Duffy, K., Zhang, X., Wang, J., Seyednasrollah, B., Gerst, K.L., 2022. Exploring discrepancies between in situ phenology and remotely derived phenometrics at NEON sites. Ecosphere 13, e3912.
Drusch, M., Del Bello, U., Carlier, S., Colin, O., Fernandez, V., Gascon, F., Hoersch, B., Isola, C., Laberinti, P., Martimort, P., Meygret, A., Spoto, F., Sy, O., Marchese, F., Bargellini, P., 2012. Sentinel-2: ESA's optical high-resolution mission for GMES operational services. Remote Sens. Environ. 120, 25–36.
Fisher, J.I., Mustard, J.F., Vadeboncoeur, M.A., 2006. Green leaf phenology at Landsat resolution: scaling from the field to the satellite. Remote Sens. Environ. 100, 265–279.
Foga, S., Scaramuzza, P.L., Guo, S., Zhu, Z., Dilley, R.D., Beckmann, T., Schmidt, G.L., Dwyer, J.L., Joseph Hughes, M., Laue, B., 2017. Cloud detection algorithm comparison and validation for operational Landsat data products. Remote Sens. Environ. 194, 379–390.
Friedl, M., Gray, J., Sulla-Menashe, D., 2019. MCD12Q2 MODIS/Terra+ Aqua Land Cover Dynamics Yearly L3 Global 500m SIN Grid V006. NASA EOSDIS Land Processes DAAC; NASA: Washington, DC, USA.
Friedl, M., 2020. MuSLI Multi-Source Land Surface Phenology Yearly North America 30 m V001. NASA EOSDIS Land Processes DAAC.
Gao, X., Gray, J.M., Reich, B.J., 2021. Long-term, medium spatial resolution annual land surface phenology with a Bayesian hierarchical model. Remote Sensing of Environment 261.
Gao, F., Zhang, X., 2021. Mapping crop phenology in near real-time using satellite remote sensing: challenges and opportunities. Journal of Remote Sensing 2021, 1–14.
Gao, F., Anderson, M.C., Zhang, X., Yang, Z., Alfieri, J.G., Kustas, W.P., Mueller, R., Johnson, D.M., Prueger, J.H., 2017. Toward mapping crop progress at field scales through fusion of Landsat and MODIS imagery. Remote Sens. Environ. 188, 9–25.
Ge, Q., Wang, H., Rutishauser, T., Dai, J., 2015. Phenological response to climate change in China: a meta-analysis. Glob Chang Biol 21, 265–274.
Gorelick, N., Hancher, M., Dixon, M., Ilyushchenko, S., Thau, D., Moore, R., 2017. Google Earth Engine: Planetary-scale geospatial analysis for everyone. Remote Sens. Environ. 202, 18–27.
Gray, J., Sulla-Menashe, D., Friedl, M.A., 2019. User guide to collection 6 modis land cover dynamics (mcd12q2) product. Missoula, MT, USA, NASA EOSDIS Land Processes DAAC.
He, Y., Dong, J., Liao, X., Sun, L., Wang, Z., You, N., Li, Z., Fu, P., 2021. Examining rice distribution and cropping intensity in a mixed single- and double-cropping region in South China using all available Sentinel 1/2 images. Int. J. Appl. Earth Obs. Geoinf. 101.
Huete, A., Didan, K., Miura, T., Rodriguez, E.P., Gao, X., Ferreira, L.G., 2002. Overview of the radiometric and biophysical performance of the MODIS vegetation indices. Remote Sens. Environ. 83, 195–213.
Jeong, S.-J., Ho, C.-H., Gim, H.-J., Brown, M.E., 2011. Phenology shifts at start vs. end of growing season in temperate vegetation over the Northern Hemisphere for the period 1982–2008. Glob. Chang. Biol. 17, 2385–2399.
Jiang, Z., Huete, A.R., Didan, K., Miura, T., 2008. Development of a two-band enhanced vegetation index without a blue band. Remote Sens. Environ. 112, 3833–3845.
Jönsson, P., Cai, Z., Melaas, E., Friedl, M., Eklundh, L., 2018. A method for robust estimation of vegetation seasonality from Landsat and Sentinel-2 time series data. Remote Sens-Basel 10.
Keenan, T.F., Gray, J., Friedl, M.A., Toomey, M., Bohrer, G., Hollinger, D.Y., Munger, J.W., O'Keefe, J., Schmid, H.P., Wing, I.S., Yang, B., Richardson, A.D., 2014. Net carbon uptake has increased through warming-induced changes in temperate forest phenology. Nat. Clim. Chang. 4, 598–604.
Li, X., Zhou, Y., Meng, L., Asrar, G.R., Lu, C., Wu, Q., 2019. A dataset of 30 m annual vegetation phenology indicators (1985–2015) in urban areas of the conterminous United States. Earth Syst Sci Data 11, 881–894.
Li, X., Cheng, G., Wang, L., Wang, J., Ran, Y., Che, T., Li, G., He, H., Zhang, Q., Jiang, X., Zou, Z., Zhao, G., 2021. Boosting geoscience data sharing in China. Nat. Geosci. 14, 541–542.
Liu, J., Kuang, W., Zhang, Z., Xu, X., Qin, Y., Ning, J., Zhou, W., Zhang, S., Li, R., Yan, C., Wu, S., Shi, X., Jiang, N., Yu, D., Pan, X., Chi, W., 2014. Spatiotemporal characteristics, patterns, and causes of land-use changes in China since the late 1980s. J. Geog. Sci. 24, 195–210.
Liu, L., Xiao, X., Qin, Y., Wang, J., Xu, X., Hu, Y., Qiao, Z., 2020. Mapping cropping intensity in China using time series Landsat and Sentinel-2 images and Google Earth Engine. Remote Sens. Environ. 239.
Masek, J.G., Wulder, M.A., Markham, B., McCorkel, J., Crawford, C.J., Storey, J., Jenstrom, D.T., 2020. Landsat 9: Empowering open science and applications through continuity. Remote Sens. Environ. 248, 111968.
Melaas, E.K., Friedl, M.A., Zhu, Z., 2013a. Detecting interannual variation in deciduous broadleaf forest phenology using Landsat TM/ETM plus data. Remote Sens. Environ. 132, 176–185.
Melaas, E.K., Friedl, M.A., Zhu, Z., 2013b. Detecting interannual variation in deciduous broadleaf forest phenology using Landsat TM/ETM+ data. Remote Sens. Environ. 132, 176–185.
Melaas, E.K., Sulla-Menashe, D., Gray, J.M., Black, T.A., Morin, T.H., Richardson, A.D., Friedl, M.A., 2016. Multisite analysis of land surface phenology in North American temperate and boreal deciduous forests from Landsat. Remote Sens. Environ. 186, 452–464.
Melaas, E.K., Sulla-Menashe, D., Friedl, M.A., 2018. Multidecadal changes and interannual variation in springtime phenology of North American temperate and boreal deciduous forests. Geophys. Res. Lett. 45, 2679–2687.
Meraner, A., Ebel, P., Zhu, X.X., Schmitt, M., 2020. Cloud removal in Sentinel-2 imagery using a deep residual neural network and SAR-optical data fusion. ISPRS J Photogramm Remote Sens 166, 333–346.
Meroni, M., d'Andrimont, R., Vrieling, A., Fasbender, D., Lemoine, G., Rembold, F., Seguini, L., Verhegghen, A., 2021. Comparing land surface phenology of major European crops as derived from SAR and multispectral data of Sentinel-1 and -2. Remote Sens Environ 253, 112232.

Migliavacca, M., Galvagno, M., Cremonese, E., Rossini, M., Meroni, M., Sonnentag, O., Cogliati, S., Manca, G., Diotri, F., Busetto, L., Cescatti, A., Colombo, R., Fava, F., Morra di Cella, U., Pari, E., Siniscalco, C., Richardson, A.D., 2011. Using digital repeat photography and eddy covariance data to model grassland phenology and photosynthetic CO2 uptake. Agric. For. Meteorol. 151, 1325–1337.
Montgomery, R.A., Rice, K.E., Stefanski, A., Rich, R.L., Reich, P.B., 2020. Phenological responses of temperate and boreal trees to warming depend on ambient spring temperatures, leaf habit, and geographic range. Proc Natl Acad Sci U S A 117, 10397–10405.
Nasrallah, A., Baghdadi, N., El Hajj, M., Darwish, T., Belhouchette, H., Faour, G., Darwich, S., Mhawej, M., 2019. Sentinel-1 Data for Winter Wheat Phenology Monitoring and Mapping. Remote Sens-Basel 11.
Niu, Q., Li, X., Huang, J., Huang, H., Huang, X., Su, W., Yuan, W., 2022. A 30 m annual maize phenology dataset from 1985 to 2020 in China. Earth Syst Sci Data 14, 2851–2864.
Pan, Z., Huang, J., Zhou, Q., Wang, L., Cheng, Y., Zhang, H., Blackburn, G.A., Yan, J., Liu, J., 2015. Mapping crop phenology using NDVI time-series derived from HJ-1 A/B data. Int. J. Appl. Earth Obs. Geoinf. 34, 188–197.
Pastick, N.J., Dahal, D., Wylie, B.K., Parajuli, S., Boyte, S.P., Wu, Z.T., 2020. Characterizing Land Surface Phenology and Exotic Annual Grasses in Dryland Ecosystems Using Landsat and Sentinel-2 Data in Harmony. Remote Sens-Basel 12.
Peng, D., Zhang, X., Zhang, B., Liu, L., Liu, X., Huete, A.R., Huang, W., Wang, S., Luo, S., Zhang, X., Zhang, H., 2017. Scaling effects on spring phenology detections from MODIS data at multiple spatial resolutions over the contiguous United States. Isprs J Photogramm 132, 185–198.
Piao, S., Fang, J., Zhou, L., Ciais, P., Zhu, B., 2006. Variations in satellite-derived phenology in China's temperate vegetation. Glob. Chang. Biol. 12, 672–685.
Piao, S., Liu, Q., Chen, A., Janssens, I.A., Fu, Y., Dai, J., Liu, L., Lian, X., Shen, M., Zhu, X., 2019. Plant phenology and global climate change: Current progresses and challenges. Glob Chang Biol 25, 1922–1940.
Qiu, T., Song, C., Li, J., 2020a. Deriving Annual Double-Season Cropland Phenology Using Landsat Imagery. Remote Sens-Basel 12.
Richardson, A.D., Keenan, T.F., Migliavacca, M., Ryu, Y., Sonnentag, O., Toomey, M., 2013. Climate change, phenology, and phenological control of vegetation feedbacks to the climate system. Agric. For. Meteorol. 169, 156–173.
Qiu, T., Song, C., Zhang, Y., Liu, H., Vose, J.M., 2020b. Urbanization and climate change jointly shift land surface phenology in the northern mid-latitude large cities. Remote Sens. Environ 236, 111477.
Richardson, A.D., Hufkens, K., Milliman, T., Aubrecht, D.M., Chen, M., Gray, J.M., Johnston, M.R., Keenan, T.F., Klosterman, S.T., Kosmala, M., Melaas, E.K., Friedl, M. A., Frolking, S., 2018a. Tracking vegetation phenology across diverse North American biomes using PhenoCam imagery. Sci Data 5, 180028.
Richardson, A.D., Hufkens, K., Milliman, T., Aubrecht, D.M., Chen, M., Gray, J.M., Johnston, M.R., Keenan, T.F., Klosterman, S.T., Kosmala, M., Melaas, E.K., Friedl, M. A., Frolking, S., 2018b. Tracking vegetation phenology across diverse North American biomes using PhenoCam imagery. Sci. Data 5.
Roy, D.P., Kovalskyy, V., Zhang, H.K., Vermote, E.F., Yan, L., Kumar, S.S., Egorov, A., 2016. Characterization of Landsat-7 to Landsat-8 reflective wavelength and normalized difference vegetation index continuity. Remote Sens Environ 185, 57–70.
Salinero-Delgado, M., Estévez, J., Pipia, L., Belda, S., Berger, K., Paredes Gómez, V., Verrelst, J., 2021. Monitoring Cropland Phenology on Google Earth Engine Using Gaussian Process Regression. Remote Sens-Basel 14.
Seyednasrollah, B., Young, A.M., Hufkens, K., Milliman, T., Friedl, M.A., Frolking, S., Richardson, A.D., Abraha, M., Allen, D.W., Apple, M., Arain, M.A., Baker, J., Baker, J.M., Baldocchi, D., Bernacchi, C.J., Bhattacharjee, J., Blanken, P., Bosch, D.D., Boughton, R., Boughton, E.H., Brown, R.F., Browning, D.M., Brunsell, N., Burns, S.P., Cavagna, M., Chu, H., Clark, P.E., Conrad, B.J., Cremonese, E., Debinski, D., Desai, A.R., Diaz-Delgado, R., Duchesne, L., Dunn, A.L., Eissenstat, D.M., El-Madany, T., Ellum, D.S.S., Ernest, S.M., Esposito, A., Fenstermaker, L., Flanagan, L.B., Forsythe, B., Gallagher, J., Gianelle, D., Griffis, T., Groffman, P., Gu, L., Guillemot, J., Halpin, M., Hanson, P.J., Hemming, D., Hove, A.A., Humphreys, E.R., Jaimes-Hernandez, A., Jaradat, A.A., Johnson, J., Keel, E., Kelly, V.R., Kirchner, J.W., Kirchner, P.B., Knapp, M., Krassovski, M., Langvall, O., Lanthier, G., Maire, G.l., Magliulo, E., Martin, T.A., McNeil, B., Meyer, G.A., Migliavacca, M., Mohanty, B.P., Moore, C.E., Mudd, R., Munger, J.W., Murrell, Z.E., Nesic, Z., Neufeld, H.S., O'Halloran, T.L., Oechel, W., Oishi, A.C., Oswald, W.W., Perkins, T.D., Reba, M.L., Rundquist, B., Runkle, B.R., Russell, E.S., Sadler, E.J., Saha, A., Saliendra, N.Z., Schmalbeck, L., Schwartz, M.D., Scott, R.L., Smith, E.M., Sonnentag, O., Stoy, P., Strachan, S., Suvocarev, K., Thom, J.E., Thomas, R.Q., Van den berg, A.K., Vargas, R., Verfaillie, J., Vogel, C.S., Walker, J.J., Webb, N., Wetzel, P., Weyers, S., Whipple, A.V., Whitham, T.G., Wohlfahrt, G., Wood, J.D., Wolf, S., Yang, J., Yang, X., Yenni, G., Zhang, Y., Zhang, Q., Zona, D., 2019b. PhenoCam Dataset v2.0: Vegetation Phenology from Digital Camera Imagery, 2000-2018. ORNL Distributed Active Archive Center.
Shen, M., Zhang, G., Cong, N., Wang, S., Kong, W., Piao, S., 2014. Increasing altitudinal gradient of spring vegetation phenology during the last decade on the Qinghai-Tibetan Plateau. Agric. For. Meteorol. 189–190, 71–80.
Seyednasrollah, B., Young, A.M., Hufkens, K., Milliman, T., Friedl, M.A., Frolking, S., Richardson, A.D., 2019a. Tracking vegetation phenology across diverse biomes using Version 2.0 of the PhenoCam Dataset. Sci. Data 6.
Shen, M., Piao, S., Cong, N., Zhang, G., Jassens, I.A., 2015. Precipitation impacts on vegetation spring phenology on the Tibetan Plateau. Glob Chang Biol 21, 3647–3656.
Tian, F., Cai, Z., Jin, H., Hufkens, K., Scheifinger, H., Tagesson, T., Smets, B., Van Hoolst, R., Bonte, K., Ivits, E., Tong, X., Ardö, J., Eklundh, L., 2021. Calibrating vegetation phenology from Sentinel-2 using eddy covariance, PhenoCam, and PEP725 networks across Europe. Remote Sensing of Environment 260.
Vitasse, Y., Baumgarten, F., Zohner, C.M., Rutishauser, T., Pietragalla, B., Gehrig, R., Dai, J., Wang, H., Aono, Y., Sparks, T.H., 2022. The great acceleration of plant phenological shifts. Nat. Clim. Chang. 12, 300–302.
Vrieling, A., Meroni, M., Darvishzadeh, R., Skidmore, A.K., Wang, T., Zurita-Milla, R., Oosterbeek, K., O'Connor, B., Paganini, M., 2018. Vegetation phenology from Sentinel-2 and field cameras for a Dutch barrier island. Remote Sens. Environ. 215, 517–529.
Wang, J., Xiao, X., Liu, L., Wu, X., Qin, Y., Steiner, J.L., Dong, J., 2020. Mapping sugarcane plantation dynamics in Guangxi, China, by time series Sentinel-1, Sentinel-2 and Landsat images. Remote Sensing of Environment 247.
Wang, J., Song, G., Liddell, M., Morellato, P., Lee, C.K.F., Yang, D., Alberton, B., Detto, M., Ma, X., Zhao, Y., Yeung, H.C.H., Zhang, H., Ng, M., Nelson, B.W., Huete, A., Wu, J., 2023. An ecologically-constrained deep learning model for tropical leaf phenology monitoring using PlanetScope satellites. Remote Sensing of Environment 286.
Wang, X.-Y., Wang, J., Jiang, Z.-Y., Li, H.-Y., Hao, X.-H., 2015. An Effective method for snow-cover mapping of dense coniferous forests in the upper heihe river basin using landsat operational land imager data. Remote Sens-Basel 7, 17246–17257.
Wang, J., Xiao, X., Zhang, Y., Qin, Y., Doughty, R.B., Wu, X., Bajgain, R., Du, L., 2018. Enhanced gross primary production and evapotranspiration in juniper-encroached grasslands. Glob. Chang. Biol. 24, 5655–5667.
Xiao, X., Boles, S., Liu, J., Zhuang, D., Frolking, S., Li, C., Salas, W., Moore, B., 2005. Mapping paddy rice agriculture in southern China using multi-temporal MODIS images. Remote Sens. Environ. 95, 480–492.
Xiao, X., Boles, S., Frolking, S., Li, C., Babu, J.Y., Salas, W., Moore, B., 2006. Mapping paddy rice agriculture in South and Southeast Asia using multi-temporal MODIS images. Remote Sens. Environ. 100, 95–113.
Xie, Q., Cleverly, J., Moore, C.E., Ding, Y., Hall, C.C., Ma, X., Brown, L.A., Wang, C., Beringer, J., Prober, S.M., Macfarlane, C., Meyer, W.S., Yin, G., Huete, A., 2022. Land surface phenology retrievals for arid and semi-arid ecosystems. Isprs J Photogramm 185, 129–145.
Xu, C., Liu, H., Williams, A.P., Yin, Y., Wu, X., 2016. Trends toward an earlier peak of the growing season in Northern Hemisphere mid-latitudes. Glob Chang Biol 22, 2852–2860.
Yang, J., Dong, J., Xiao, X., Dai, J., Wu, C., Xia, J., Zhao, G., Zhao, M., Li, Z., Zhang, Y., Ge, Q., 2019. Divergent shifts in peak photosynthesis timing of temperate and alpine grasslands in China. Remote Sensing of Environment 233.
Yang, J., Xiao, X., Doughty, R., Zhao, M., Zhang, Y., Köhler, P., Wu, X., Frankenberg, C., Dong, J., 2022. TROPOMI SIF reveals large uncertainty in estimating the end of plant growing season from vegetation indices data in the Tibetan Plateau. Remote Sens. Environ. 280, 113209.
You, N., Dong, J., Huang, J., Du, G., Zhang, G., He, Y., Yang, T., Di, Y., Xiao, X., 2021. The 10-m crop type maps in Northeast China during 2017–2019. Sci Data 8, 41.
Zeng, Z., Piao, S., Li, L.Z.X., Zhou, L., Ciais, P., Wang, T., Li, Y., Lian, X., Wood, E.F., Friedlingstein, P., Mao, J., Estes, L.D., Myneni, R.B., Peng, S., Shi, X., Seneviratne, S. I., Wang, Y., 2017. Climate mitigation from vegetation biophysical feedbacks during the past three decades. Nat. Clim. Chang. 7, 432–436.
Zhang, X., Friedl, M., Henebry, G.M., 2020a. VIIRS/NPP Land Cover Dynamics Yearly L3 Global 500m SIN Grid V001, in: DAAC, N.E.L.P. (Ed.), distributed by NASA EOSDIS Land Processes DAAC.
Zhang, X., Xiao, X., Qiu, S., Xu, X., Wang, X., Chang, Q., Wu, J., Li, B., 2022. Quantifying latitudinal variation in land surface phenology of Spartina alterniflora saltmarshes across coastal wetlands in China by Landsat 7/8 and Sentinel-2 images. Remote Sensing of Environment 269.
Zhang, X.Y., Jayavelu, S., Liu, L.L., Friedl, M.A., Henebry, G.M., Liu, Y., Schaaf, C.B., Richardson, A.D., Gray, J., 2018c. Evaluation of land surface phenology from VIIRS data using time series of PhenoCam imagery. Agric. For. Meteorol. 256, 137–149.
Zhang, X., Wang, J., Gao, F., Liu, Y., Schaaf, C., Friedl, M., Yu, Y., Jayavelu, S., Gray, J., Liu, L., Yan, D., Henebry, G.M., 2017. Exploration of scaling effects on coarse resolution land surface phenology. Remote Sens. Environ. 190, 318–330.
Zhang, X., Liu, L., Henebry, G.M., 2019. Impacts of land cover and land use change on long-term trend of land surface phenology: a case study in agricultural ecosystems. Environ Res Lett 14.
Zhang, X., Liu, L., Chen, X., Gao, Y., Xie, S., Mi, J., 2021b. GLC_FCS30: global land-cover product with fine classification system at 30 m using time-series Landsat imagery. Earth Syst. Sci. Data 13, 2753–2776.
Zhang, X., Liu, L., Liu, Y., Jayavelu, S., Wang, J., Moon, M., Henebry, G.M., Friedl, M.A., Schaaf, C.B., 2018b. Generation and evaluation of the VIIRS land surface phenology product. Remote Sens. Environ. 216, 212–229.
Zhang, H.K., Roy, D.P., Yan, L., Li, Z., Huang, H., Vermote, E., Skakun, S., Roger, J.-C., 2018a. Characterization of Sentinel-2A and Landsat-8 top of atmosphere, surface, and nadir BRDF adjusted reflectance and NDVI differences. Remote Sens. Environ. 215, 482–494.
Zhang, X., Wang, J., Henebry, G.M., Gao, F., 2020b. Development and evaluation of a new algorithm for detecting 30 m land surface phenology from VIIRS and HLS time series. Isprs J Photogramm 161, 37–51.
Zhang, M., Wu, B., Zeng, H., He, G., Liu, C., Tao, S., Zhang, Q., Nabil, M., Tian, F., Bofana, J., Beyene, A.N., Elnashar, A., Yan, N., Wang, Z., Liu, Y., 2021a. GCI30: a global dataset of 30 m cropping intensity using multisource remote sensing imagery. Earth Syst Sci Data 13, 4799–4817.
Zhao, Y., Lee, C.K.F., Wang, Z., Wang, J., Gu, Y., Xie, J., Law, Y.K., Song, G., Bonebrake, T.C., Yang, X., Nelson, B.W., Wu, J., 2022. Evaluating fine-scale

phenology from PlanetScope satellites with ground observations across temperate forests in eastern North America. Remote Sensing of Environment 283, 113310.

Zhou, Y., 2022. Understanding urban plant phenology for sustainable cities and planet. Nat. Clim. Chang. 12, 302–304.

Zhu, Z., Wang, S., Woodcock, C.E., 2015. Improvement and expansion of the Fmask algorithm: cloud, cloud shadow, and snow detection for Landsats 4–7, 8, and Sentinel 2 images. Remote Sens. Environ. 159, 269–277.